

Sequence-Impedance-Based Harmonic Stability Analysis and Controller Parameter Design of Three-Phase Inverter-Based Multibus AC Power Systems

Wenchao Cao, *Student Member, IEEE*, Yiwei Ma, *Student Member, IEEE*, and Fred Wang, *Fellow, IEEE*

Abstract—Three-phase inverter-based multibus ac power systems could suffer from the harmonic instability issue. The existing impedance-based stability analysis method using the Nyquist stability criterion once requires the calculation of right-half-plane (RHP) poles of impedance ratios, which would result in a heavy computation burden for complicated systems. In order to analyze the harmonic stability of multibus ac systems consisting of both voltage-controlled and current-controlled inverters without the need for RHP pole calculation, this paper proposes two sequence-impedance-based harmonic stability analysis methods. Based on the summary of all major connection types including mesh, the proposed Method 1 can analyze the harmonic stability of multibus ac systems by adding the components one by one from nodes in the lowest level to areas in the highest system level, and accordingly, applying the stability criteria multiple times in succession. The proposed Method 2 is a generalized extension of the impedance-sum-type criterion to be used for the harmonic stability analysis of any multibus ac systems based on Cauchy's theorem. The inverter controller parameters can be designed in the forms of stability regions in the parameter space, by repetitively applying the proposed harmonic stability analysis methods. Experimental results of inverter-based multibus ac systems validate the effectiveness of the proposed harmonic stability analysis methods and parameter design approach.

Index Terms—Harmonic stability, impedance-based analysis, inverter-based system, Nyquist stability criterion.

I. INTRODUCTION

POWER electronics converters are widely used for energy conversion in three-phase ac systems, such as renewable energy systems [1], microgrids [2], electric railway systems

[3], electric aircrafts [4], and modern electric ships [5]. These power electronics converters-based three-phase ac systems may suffer from small-signal instability issues due to the dynamic interactions among the converters and passive components in the systems [6]–[8]. The small-signal instability issues can be divided into two categories in different frequency ranges [9]: 1) unstable harmonic resonances, which result from the interactions among the fast inner current or voltage control loops, converter output filters, and network passive components [9], [10]; and 2) low-frequency oscillations, which arise from the interactions among the slow outer power control loops and grid synchronization loops [11]–[13]. It is crucial for system integrators to analyze the system stability and design the converter controller parameters during system planning and maintenance periods to guarantee stable system operation [13], [14]. The focus of this paper is on the harmonic instability issues instead of the low-frequency oscillation problems.

There are several approaches to analyze the small-signal stability of three-phase multibus ac systems consisting of multiple three-phase inverters. Compared with the approaches using the state-space model [15], [16] or the closed-loop transfer function matrix model [17] of the whole system, the impedance-based approach, based on the ratio of the impedances of two subsystems at the interface, has the potential advantage to clearly interpret the impact of individual components or subsystems on the system stability [9]. There are generally two kinds of impedance models for three-phase balanced ac systems [18]–[20], that is, the dq impedance matrix model in the synchronous dq frame [21] and the harmonic-linearization-based sequence impedance model [22]. The dq impedance models can be used to assess both the harmonic instability and low-frequency oscillation problems by using the generalized Nyquist stability criterion (GNC) [23]–[26], but the manipulation of dq impedance matrices is complicated. As reported in [27] and [28], the positive-sequence and negative-sequence impedances of inverters are decoupled, if 1) only inner current or voltage loops with symmetric structures and equal parameters in d - and q -axis are considered, and 2) no phase-locked loop (PLL) is adopted or the PLL has negligible impact due to a sufficiently low bandwidth. Under these conditions of decoupling, the sequence impedance models have been proven to be effective in analyzing the harmonic

Manuscript received May 17, 2016; revised August 24, 2016 and October 20, 2016; accepted November 22, 2016. Date of publication December 9, 2016; date of current version May 9, 2017. This work was supported by the Engineering Research Center Program of the National Science Foundation and the Department of Energy under NSF Award EEC-1041877, and by the CURENT Industry Partnership Program. Recommended for publication by Associate Editor M. S. ElMoursi.

The authors are with the Center for Ultra-Wide-Area Resilient Electric Energy Transmission Networks, Department of Electrical Engineering and Computer Science, College of Engineering, The University of Tennessee, Knoxville, TN 37996-2250 USA (e-mail: wcao2@vols.utk.edu; yma13@vols.utk.edu; fred.wang@utk.edu).

Color versions of one or more of the figures in this paper are available online at <http://ieeexplore.ieee.org>.

Digital Object Identifier 10.1109/TPEL.2016.2637883

stability based on the Nyquist stability criterion [9], [10], [22], [29]. Considering that the scalar computation of decoupled positive-sequence and negative-sequence impedances under above conditions is simple, this paper focuses on sequence impedances and the Nyquist stability criterion for harmonic stability analysis of three-phase multibus ac systems.

When using the Nyquist stability criterion or GNC, not only the encirclement of the Nyquist plot around $(-1, j0)$ should be examined, but also the right-half-plane (RHP) poles of the impedance ratio or return ratio matrix should be checked [23], [30]. For converter-based ac systems that could be divided into a stable source subsystem and a stable load subsystem, the ratio of two subsystems' impedances does not have RHP poles, and, thus, the pole examination is avoided in the stability analysis. This applies to the systems with simple structures, such as grids with a single inverter [19], [22] or directly paralleled multiple inverters [10], [13], [31], and source-load systems with one common ac bus [14], [25], [26], [32]. However, for complicated inverter-based ac systems with multiple buses, such as meshed power systems [9] and microgrids [11], normally they could not be easily divided into two stable subsystems during the system planning stage, and, therefore, it is necessary to exam the RHP poles of the impedance ratio when using the Nyquist stability criterion or GNC for stability analysis, which requires detailed transfer function models of components and would result in a heavy computation burden for complicated systems.

A number of research efforts have been made to avoid the pole calculation of the impedance ratio and facilitate the impedance-based stability analysis of inverter-based multibus systems. The harmonic stability of a three-phase meshed power system made up of multiple voltage-controlled and current-controlled inverters was evaluated in [9], by analyzing the Nyquist plot of the impedance ratio at each point of connection (PoC) of component. However, the stability analysis at different PoCs of components could reveal conflictive results [31]. A conservative regional impedance-based stability analysis method was proposed in [33] for a radial distribution network with multiple current-controlled inverters, by analyzing the stability step by step from the simplest entity to the entire network. Nevertheless, systems with voltage-controlled inverters or meshed connections are not considered in [33]. Some other stability criteria were also reported, such as the impedance-sum-type criterion [34] and the Nyquist criterion for multiloop system [35]. However, these methods are only applicable to paralleled source-source converter systems with only voltage-controlled converters or only current-controlled converters instead of the mix of both types.

As for converter controller design for system stability, one way is to shape the converter impedance by emulating virtual impedance [36], [37] or inserting filters into control loops [38], [39], which relies on the knowledge of system impedances or resonance frequency information. Another way is to make the converter impedance passive based on frequency-domain passivity theory, by adjusting controller parameters or adding special controllers [18], [40]–[42], but the passivity-based design requires a tradeoff between dynamic performance and passivity. A third way is to select proper controller parameters based on the system stability analysis [25], [43]. Proper controller

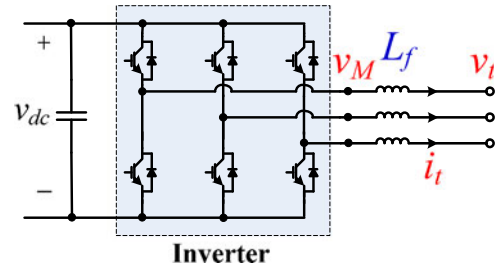


Fig. 1. Block diagram of a three-phase inverter with an output L filter.

parameter ranges can be determined to meet the specified stability margin requirements [43], [44], or they can be presented as stability regions and boundaries in the parameter space [12], [45]. For simple source-load systems, given the load-side impedance, it is relatively easy to design the controller parameters of the source side by adjusting its impedance to meet the impedance-based stability criteria, or vice versa [25], [43]. However, for inverter-based multibus ac systems, it is not easy to design the controller parameters of each inverter individually due to the interconnection of all inverters.

The objective of this paper is to analyze the small-signal harmonic stability and design the inverter controller parameters for three-phase multibus ac systems consisting of both voltage-controlled and current-controlled inverters. Two harmonic stability analysis methods based on inverter sequence impedances in positive- and negative-sequence domains are proposed to avoid the examination of the RHP poles of the impedance ratios and reduce the computation burden as compared to the existing analysis method using the Nyquist stability criterion once. In addition, the proposed methods enable the system stability assessment using only the measured terminal impedance characteristics instead of internal control details of system components. The controller parameters are further designed to guarantee system stability, by repetitively applying the proposed stability analysis methods in the whole possible parameter ranges to obtain the stable regions in the parameter space. Experimental results of two inverter-based multibus ac systems, namely a two-area system and a meshed system, composed of both voltage-controlled and current-controlled inverters demonstrate the effectiveness of the proposed approach.

II. SEQUENCE IMPEDANCE MODELING OF THREE-PHASE INVERTERS

The block diagram of the three-phase inverter with an output L filter is shown in Fig. 1, where i_t is the inverter output current, v_M is the inverter output voltage, and v_t is the inverter terminal voltage. For the analysis of harmonic stability problems, the dc-link voltage v_{dc} can be assumed as constant, because it is regulated by a front-end converter or the bandwidth of the v_{dc} control is lower than the system fundamental frequency [9]. This paper only focuses on the harmonic instability issues instead of the low-frequency oscillation problems. Therefore, only the inner voltage and current-control loops with symmetric structures and equal parameters in d - and q -axis are considered

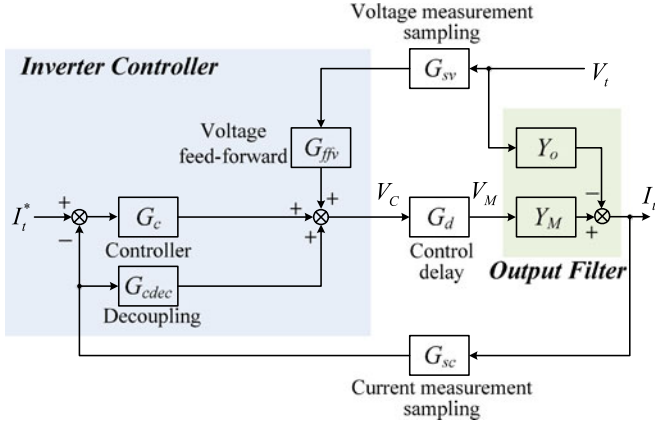


Fig. 2. Block diagram of the current-control loop in the sequence domain.

here for harmonic stability analysis, and the outer power control loops and droop control loops are not modeled, and, thus, the low-frequency power oscillations are disregarded. In addition, a basic PLL is usually used to obtain the angle θ_1 and frequency ω_1 information of the inverter terminal voltage v_t . When the PLL bandwidth is small (such as 10 Hz used in this paper), the PLL has a negligible impact in the frequency range above 100 Hz. Therefore, for the sake of harmonic stability analysis, the PLL is not considered in the following models, and the positive- and negative-sequence impedances or admittances of inverters can be regarded as decoupled [27], [28].

A. Sequence Admittances of Current-Controlled Inverters

The block diagram of the current-control loop in the sequence domain can be depicted in Fig. 2 [46]. The output L filter can be modeled by two admittances Y_M and Y_o represented by (1), where L_f and R_{Lf} are the inductance and resistance of the L filter, respectively. The sampling processes of the voltage and current are modeled as two 0.5-switching period (T_s) delay units G_{sv} and G_{sc} , respectively, and G_d is the approximately delay of $1.5T_s$ introduced in the digital control, as shown in (2)

$$Y_M = Y_o = \frac{1}{L_f s + R_{Lf}} \quad (1)$$

$$G_{sv} = G_{sc} = e^{-0.5T_s s}, \quad G_d = e^{-1.5T_s s}. \quad (2)$$

The transfer functions of the control gains inside the “inverter controller” block in Fig. 2 are expressed as (3) in the dq frame. $G_c(s)$ is the transfer function of the proportional plus integral (PI) controller, with the proportional gain K_{cp} and the integral gain K_{ci} . $G_{cdec}(s)$ is the transfer function of the decoupling term. A first-order low-pass filter with the cutoff frequency ω_{ffv} is used as the voltage feedforward gain $G_{ffv}(s)$. To derive the output admittance of the inverter in the sequence domain, all the control gains are converted from their transfer functions in the dq frame to the corresponding transfer functions in the positive-sequence domain as expressed in (4) and the negative-sequence

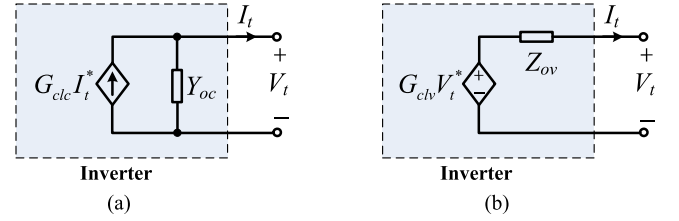


Fig. 3. (a) Norton equivalent circuit of a current-controlled inverter in the sequence domain. (b) Thevenin equivalent circuit of a voltage-controlled inverter in the sequence domain.

TABLE I
ELECTRICAL PARAMETERS OF THE INVERTERS

Electrical Parameters	Values	
L filter	L_f	0.575 mH
	R_{Lf}	0.2 Ω
DC-link voltage	V_{dc}	130 V
AC grid voltage	V_g	50 V (phase peak)
Inverter rated current	I_{rated}	20 A
Fundamental frequency	ω_1	$60 \times 2\pi$ rad/s

domain as shown in (5) [22], [46]

$$G_c(s) = K_{cp} + \frac{K_{ci}}{s},$$

$$G_{cdec}(s) = \omega_1 L_f, \quad G_{ffv}(s) = \frac{1}{1 + s/\omega_{ffv}} \quad (3)$$

$$G_c = G_c(s - j\omega_1), \quad G_{cdec} = j\omega_1 L_f,$$

$$G_{ffv} = G_{ffv}(s - j\omega_1) \quad (4)$$

$$G_c = G_c(s + j\omega_1),$$

$$G_{cdec} = -j\omega_1 L_f, \quad G_{ffv} = G_{ffv}(s + j\omega_1). \quad (5)$$

The open-loop gain T_c and the closed-loop gain G_{clc} of the current-control loop as well as the closed-loop output admittance Y_{oc} of the inverter, as defined in (6), can be derived from the block diagram shown in Fig. 2 in both the positive- and negative-sequence domains. The Norton equivalent circuit of a current-controlled inverter is depicted in Fig. 3(a)

$$\begin{cases} T_c = (G_c - G_{cdec}) G_d Y_M G_{sc}, & G_{clc} = \frac{I_t}{I_t^*} = \frac{G_c G_d Y_M}{1 + T_c} \\ Y_{oc} = -\frac{I_t}{V_t} = \frac{Y_o - G_{sv} G_d Y_M G_{ffv}}{1 + T_c} \end{cases} \quad (6)$$

For an inverter with parameters shown in Tables I and II and output current $I_{td} = -15$ A, $I_{tq} = 0$ A, Fig. 4 shows the Bode plots of the positive-sequence admittance $Y_{oc,p}(s)$ and negative-sequence admittance $Y_{oc,n}(s)$. The difference between the analytical results and experimental measurement results in the frequency range below 100 Hz is mainly due to the neglect of the PLL in the analytical models [46]. In addition, it can be observed that $Y_{oc,p}(s)$ and $Y_{oc,n}(s)$ are different in the frequency range below 1000 Hz, which is caused by the different transfer

TABLE II
CONTROLLER PARAMETERS OF CURRENT-CONTROLLED INVERTERS

Controller Parameters		Values
Switching frequency	f_s	10 kHz
Switching period	T_s	100 μ s
Current controller	K_{cp}	2.6
	K_{ci}	2275
Voltage feedforward	ω_{fv}	$50 \times 2\pi$ rad/s

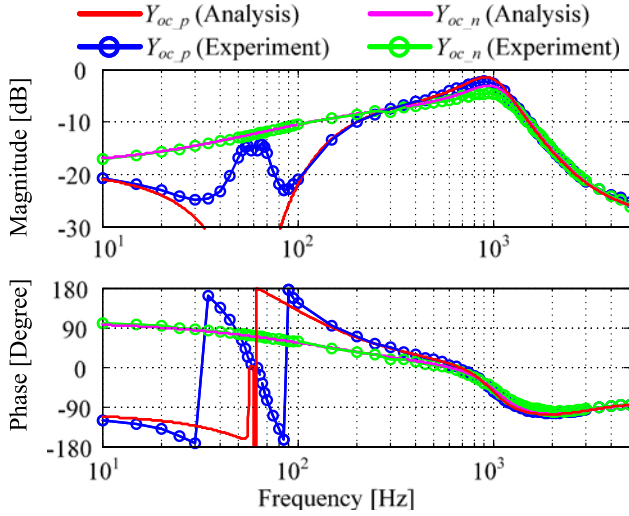


Fig. 4. Positive- and negative-sequence admittances of an inverter with PI current control in the dq frame.

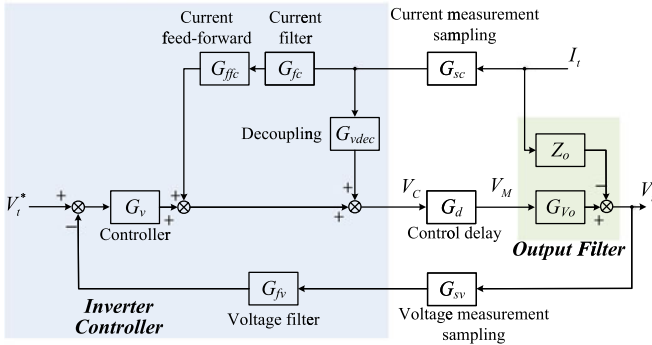


Fig. 5. Block diagram of the voltage control loop in the sequence domain.

functions of control gains in the positive- and negative-sequence domains as expressed in (4) and (5), respectively.

B. Sequence Impedances of Voltage-Controlled Inverters

For voltage-controlled three-phase inverters with a PI voltage controller and the current-feedforward control in the synchronous dq frame [47], the block diagram of the voltage control loop in the sequence domain can be illustrated in Fig. 5. The output L filter can be modeled by a voltage gain G_{Vo} and an impedance Z_o represented by (7). The transfer functions of the control gains inside the “inverter controller” block in the dq frame are explained as follows. $G_v(s)$ is the PI voltage controller

TABLE III
CONTROLLER PARAMETERS OF VOLTAGE-CONTROLLED INVERTERS

Controller Parameters		Values
Switching frequency	f_s	10 kHz
Switching period	T_s	100 μ s
Voltage controller	K_{vp}	1.04
	K_{vi}	325
Current filter	ω_{fc}	$1000 \times 2\pi$ rad/s
Voltage filter	ω_{fv}	$300 \times 2\pi$ rad/s

with proportional gain K_{vp} and integral gain K_{vi} . $G_{vdec}(s)$ is the decoupling term. $G_{fv}(s)$ and $G_{fc}(s)$ are first-order low-pass voltage filter and current filter, with ω_{fv} and ω_{fc} as the cutoff frequencies, respectively. $G_{ffc}(s)$ is the current feedforward gain. The transfer functions of these control gains are expressed in (8) in the dq frame, while the corresponding transfer functions are expressed in (9) in the positive-sequence domain and expressed in (10) in the negative-sequence domain

$$G_{Vo} = 1, \quad Z_o = L_f s + R_{Lf} \quad (7)$$

$$\begin{cases} G_v(s) = K_{vp} + \frac{K_{vi}}{s}, & G_{vdec}(s) = \omega_1 L_f \\ G_{fv}(s) = \frac{1}{1+s/\omega_{fv}}, & G_{fc}(s) = \frac{1}{1+s/\omega_{fc}}, & G_{ffc}(s) = L_f s \end{cases} \quad (8)$$

$$\begin{cases} G_v = G_v(s - j\omega_1), & G_{vdec} = j\omega_1 L_f, & G_{fv} = G_{fv}(s - j\omega_1) \\ G_{fc} = G_{fc}(s - j\omega_1), & G_{ffc} = G_{ffc}(s - j\omega_1) \end{cases} \quad (9)$$

$$\begin{cases} G_v = G_v(s + j\omega_1), & G_{vdec} = -j\omega_1 L_f, & G_{fv} = G_{fv}(s + j\omega_1) \\ G_{fc} = G_{fc}(s + j\omega_1), & G_{ffc} = G_{ffc}(s + j\omega_1) \end{cases} \quad (10)$$

The open-loop gain T_v and the closed-loop gain G_{clv} of the voltage-control loop as well as the closed-loop output impedance Z_{ov} of the inverter can be derived as (11) in both the positive- and negative-sequence domains. The Thevenin equivalent circuit of a voltage-controlled inverter is shown in Fig. 3(b). For an inverter with parameters listed in Tables I and III and output voltage $V_{td} = 50$ V, $V_{tq} = 0$ V, Fig. 6 shows the analytical results and simulation measurement results of the positive-sequence impedance $Z_{ov,p}(s)$ and negative-sequence impedance $Z_{ov,n}(s)$. The difference between $Z_{ov,p}(s)$ and $Z_{ov,n}(s)$ in the frequency range below 1000 Hz is mainly due to the different transfer functions of control gains in the positive- and negative-sequence domains as expressed in (9) and (10), respectively

$$\begin{cases} T_v = G_v G_d G_{Vo} G_{sv} G_{fv}, & G_{clv} = \frac{V_t}{V_t^*} = \frac{G_v G_d G_{Vo}}{1 + T_v} \\ Z_{ov} = -\frac{V_t}{I_t} = \frac{Z_o - G_{sc} G_d G_{Vo} (G_{vdec} + G_{fc} G_{ffc})}{1 + T_v} \end{cases} \quad (11)$$

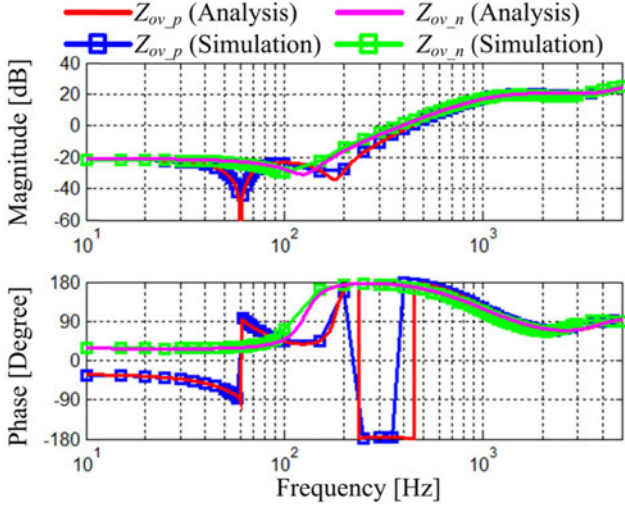


Fig. 6. Positive- and negative-sequence impedances of an inverter with PI voltage control in the dq frame.

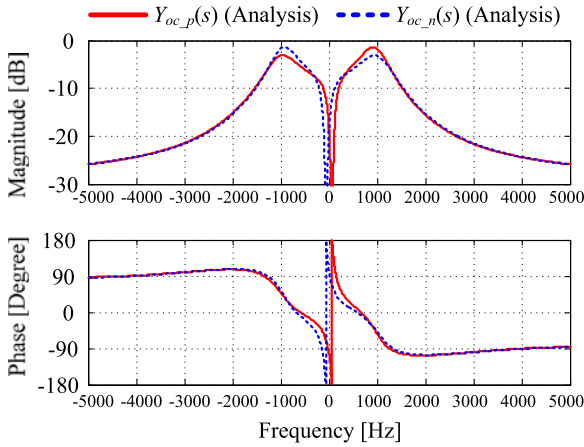


Fig. 7. Positive- and negative-sequence admittances of a current-controlled inverter in the full frequency range.

C. Discussion on Sequence Impedance Models

1) *Sequence Impedance Models in the Full Frequency Range:* As expressed in (6) and (11), the positive-sequence and negative-sequence admittances ($Y_{oc,p}(s)$ and $Y_{oc,n}(s)$) or impedances ($Z_{ov,p}(s)$ and $Z_{ov,n}(s)$) of inverters are complex transfer functions. Figs. 4 and 6 only show the Bode plots of sequence admittances or impedances of inverters in the positive frequency range $(0, +\infty)$. Figs. 7 and 8 further depict the sequence admittances or impedances of inverters in the full frequency range $(-\infty, +\infty)$. It can be observed that the Bode plot of each of $Y_{oc,p}(s)$, $Y_{oc,n}(s)$, $Z_{ov,p}(s)$, and $Z_{ov,n}(s)$ is approximately antisymmetric in the full frequency range $(-\infty, +\infty)$, with approximately equal magnitudes but opposite phases. In the following sections, Nyquist diagrams of an impedance ratio in the sequence domains are drawn in the full frequency range $(-\infty, +\infty)$, in order to clearly illustrate the encirclement of the critical point $(-1, j0)$. Nevertheless, considering the approximate antisymmetric Bode plots of sequence impedances,

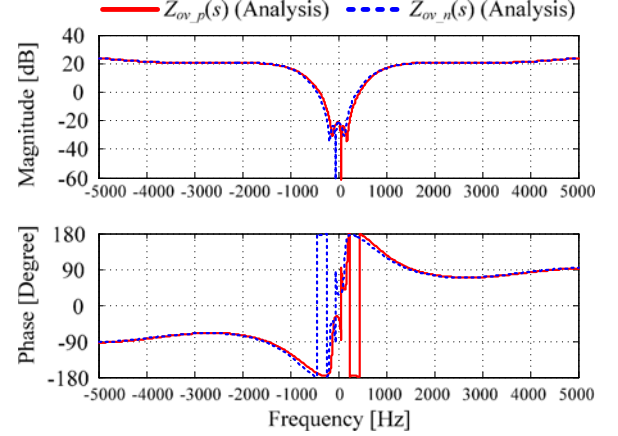


Fig. 8. Positive- and negative-sequence impedances of a voltage-controlled inverter in the full frequency range.

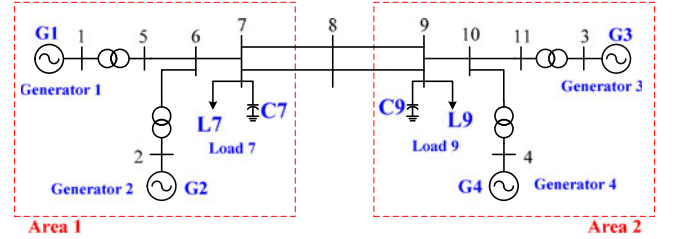


Fig. 9. One-line diagram of the two-area system.

Bode plots of a function of sequence impedances are drawn only in the positive frequency range $(0, +\infty)$ to clearly demonstrate the net phase change or the encirclement of the origin point $(0, j0)$.

2) *With LCL Filters:* Due to the actual experimental setup, only the L filters are considered in this paper. Other high-order filters with small volumes, such as LCL filters, are also commonly used in practice. The output sequence impedance models of inverters with LCL filters are different from the models presented here, but they were studied in the existing literature [9], [48]. In addition, the focus of this paper is on the system-level harmonic stability analysis, the analysis and parameter design methods developed in this paper are applicable to the systems consisting of inverters with LCL filters.

III. SMALL-SIGNAL HARMONIC STABILITY ANALYSIS

A. System Description

Fig. 9 depicts the one-line diagram of a two-area system [15], which is a typical system used for power-system related research. Fig. 10 illustrates a one-line diagram of an inverter-based multibus ac system for scaled-down emulation of the two-area system, where four generators G1–G4 are replaced by four voltage-controlled inverters [47] and two loads L7 and L9 are replaced by two current-controlled inverters [49]. The dc-link voltages of all inverters are regulated as constant by front-end dc power supplies. The parameters of the inverters are the same, which are shown in Table I. The main circuit parameters

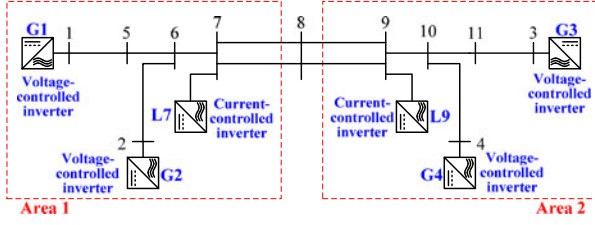


Fig. 10. One-line diagram of an inverter-based multibus ac system for scaled-down emulation of the two-area system.

TABLE IV
ELECTRICAL PARAMETERS OF THE SCALED-DOWN TWO-AREA SYSTEM

Electrical Parameters		Values
AC voltage base	V_{base}	50 V (phase peak)
AC current base	I_{base}	17.36 A
AC power base	S_{base}	1302 W
Line impedances	$Z_{1-6} (L_{1-6}, R_{1-6})$	2.45 mH, 0.12 Ω
	$Z_{2-6} (L_{2-6}, R_{2-6})$	1.2 mH, 0.04 Ω
	$Z_{6-7} (L_{6-7}, R_{6-7})$	0.7 mH, 0.035 Ω
	$Z_{7-9} (L_{7-9}, R_{7-9})$	10.7 mH, 0.65 Ω
	$Z_{3-10} (L_{3-10}, R_{3-10})$	2.5 mH, 0.12 Ω
	$Z_{4-10} (L_{4-10}, R_{4-10})$	0.7 mH, 0.04 Ω
	$Z_{9-10} (L_{9-10}, R_{9-10})$	0.7 mH, 0.035 Ω

TABLE V
OPERATING POINT OF THE SCALED-DOWN TWO-AREA SYSTEM

Operating Point		Values
Current references of each current-controlled inverter	I_d	-10 A
	I_q	0 A
Voltage references of each voltage-controlled inverter	V_d	50 V
	V_q	0 V

and operating points of the system are given in Tables IV and V. Only the inner voltage and current-control loops of these inverters are considered for harmonic stability analysis in this paper, while the low-bandwidth outer generator emulation and load emulation control loops [47], [49] are neglected.

B. Existing Stability Analysis Method: Using Nyquist Stability Criterion Once

The impedance-based equivalent circuit of the studied inverter-based multibus ac system in the sequence domain is shown in Fig. 11. The multibus system can be divided into two subsystems at any bus, where the rank of the controllability and observability matrices is full [23], such as Bus 1 or Bus 7, for harmonic stability analysis. For example, assume the system is divided at Bus 7. The total sequence admittances Y_{B7L} of the left-side subsystem and Y_{B7R} of the right-side subsystem can be obtained by forcing the voltage sources and current sources to zero. The expressions of Y_{B7L} and Y_{B7R} are shown in (12) and (13). The impedance ratio $T_{m.B7}$ (also called the minor loop gain) and the closed minor loop gain $T_{clm.B7}$ of the impedance ratio at Bus 7 are expressed in (14). The impedance Z_{lk} of each line is expressed in (15) with the line inductance L_{lk} and

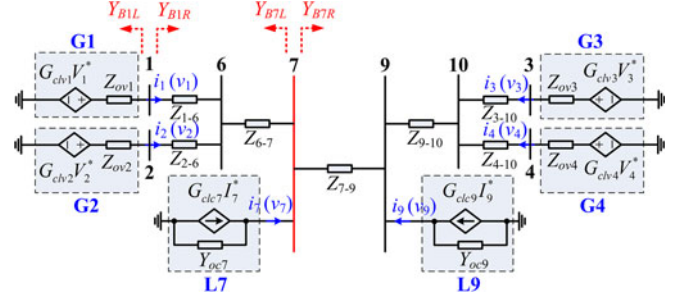


Fig. 11. Impedance-based equivalent circuit of the studied system in the sequence domain.

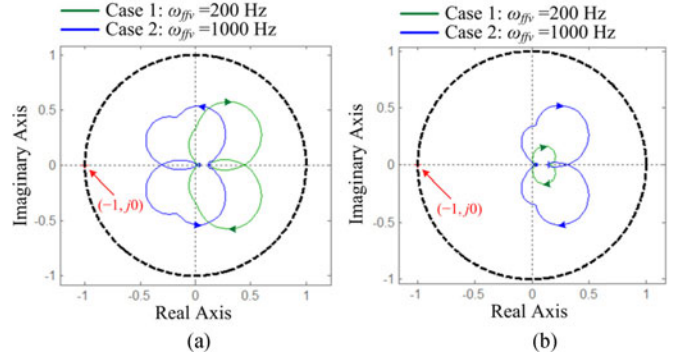


Fig. 12. Nyquist diagrams of the impedance ratios in Case 1 and Case 2 in the full frequency range: (a) $T_{m.B7.p}(s)$ and (b) $T_{m.B7.n}(s)$.

resistance R_{lk}

$$Y_{B7L} = Y_{oc7} + \frac{1}{Z_{6-7} + \frac{1}{\frac{1}{Z_{ov1} + Z_{1-6}} + \frac{1}{Z_{ov2} + Z_{2-6}}}} \quad (12)$$

$$Y_{B7R} = \frac{1}{Z_{7-9} + \frac{1}{Y_{oc9} + \frac{1}{Z_{9-10} + \frac{1}{\frac{1}{Z_{ov3} + Z_{3-10}} + \frac{1}{Z_{ov4} + Z_{4-10}}}}}} \quad (13)$$

$$T_{m.B7} = \frac{Y_{B7R}}{Y_{B7L}}, \quad T_{clm.B7} = \frac{1}{1 + T_{m.B7}} = \frac{1}{1 + \frac{Y_{B7R}}{Y_{B7L}}} \quad (14)$$

$$Z_{lk} = L_{lk}s + R_{lk}. \quad (15)$$

Then, the system stability can be assessed by applying the Nyquist stability criterion to the impedance ratio, which can be described as

$$P(T_{clm.B7}) = Z(1 + T_{m.B7}) = P(T_{m.B7}) - N_{(-1, j0)}(T_{m.B7}) \quad (16)$$

where $P()$ and $Z()$ denote the numbers of RHP poles and zeros respectively, $N_{(-1, j0)}()$ is the number of times that the Nyquist trajectory encircles the critical point $(-1, j0)$ in an anticlockwise direction. The system is stable if and only if $Z(1 + T_{m.B7})$ is zero. According to the Nyquist stability criterion, not only the Nyquist diagram but also the RHP poles of the impedance ratio should be examined to evaluate the system stability. Furthermore, the total system is stable only if both the

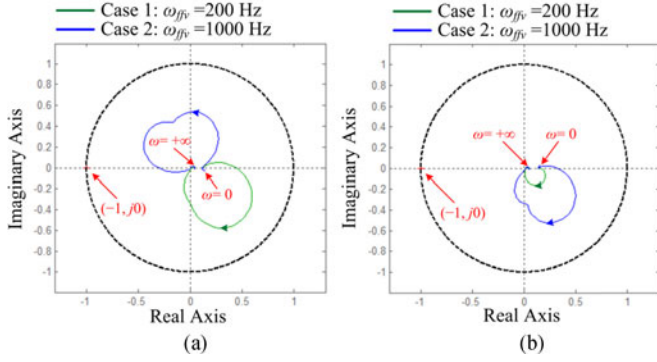


Fig. 13. Nyquist diagrams of the impedance ratios in Case 1 and Case 2 in the positive frequency range: (a) $T_{m.B7.p}(s)$ and (b) $T_{m.B7.n}(s)$.

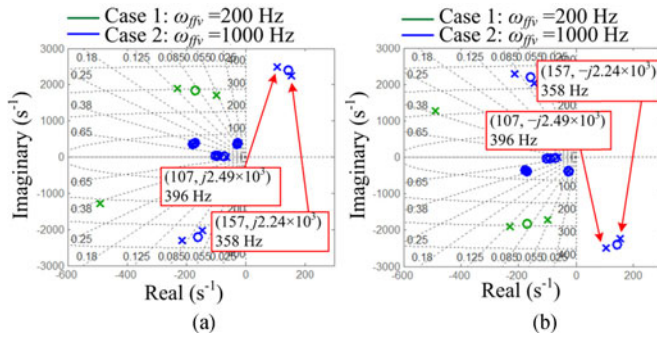


Fig. 14. Pole-zero maps of the impedance ratios in Case 1 and Case 2: (a) $T_{m.B7.p}(s)$ and (b) $T_{m.B7.n}(s)$.

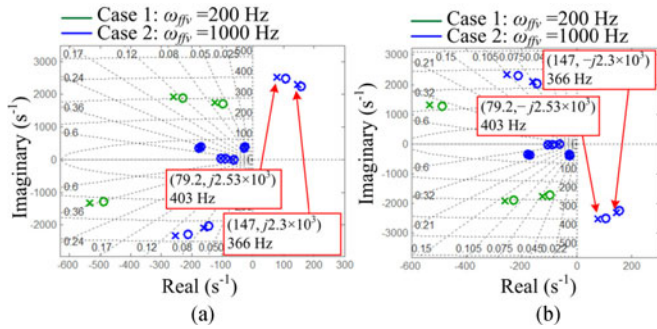


Fig. 15. Pole-zero maps of the closed loop gains of impedance ratios in Case 1 and Case 2: (a) $T_{clm.B7.p}(s)$ and (b) $T_{clm.B7.n}(s)$.

positive-sequence impedance ratio $T_{m.B7.p}(s)$ and the negative-sequence impedance ratio $T_{m.B7.n}(s)$ meet the Nyquist stability criterion. It should be noted that the system stability can also be assessed by the RHP poles of the closed-loop gain $T_{clm.B7}$ in both the positive-sequence domain $T_{clm.B7.p}(s)$ and the negative-sequence domain $T_{clm.B7.n}(s)$.

The voltage feedforward control has a potential destabilizing effect on the inverter stability [40], [44], [50]. The cutoff frequency parameter ω_{ffv} of the voltage feedforward gain G_{ffv} of all the current-controlled inverters is selected as an example to investigate its impact on the system stability. Two cases are investigated. Case 1: $\omega_{ffv} = 200 \times 2\pi$ rad/s; Case 2:

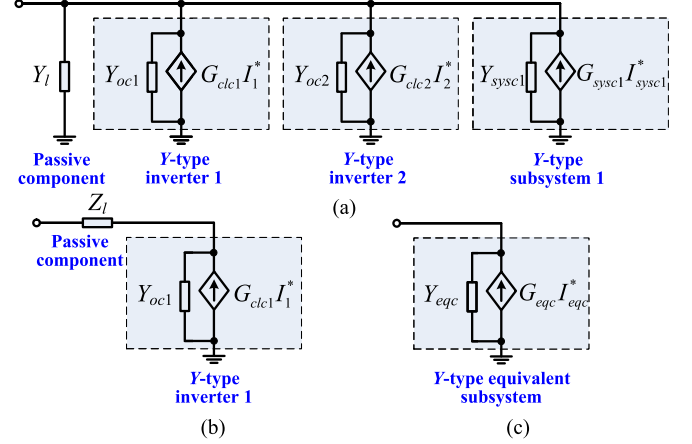


Fig. 16. System connection and equivalent circuit. (a) Y+Y parallel-type connection; (b) Y+Z series-type connection; and (c) Y-type equivalent subsystem.

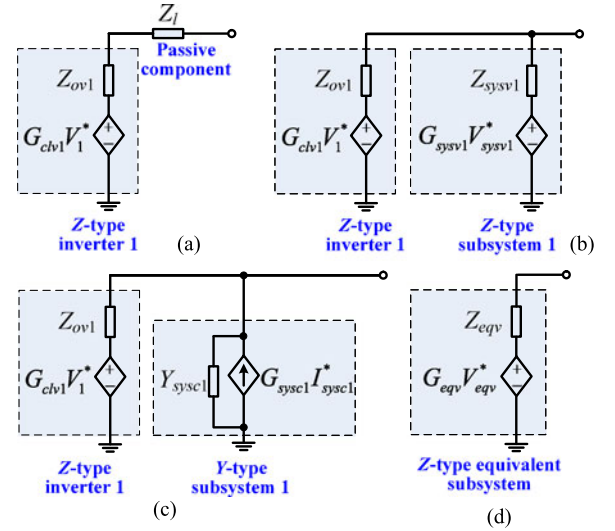


Fig. 17. System connection and equivalent circuit. (a) Z+Z series-type connection; (b) Z+Z parallel-type connection; (c) Z+Y parallel-type connection; and (d) Z-type equivalent subsystem.

$\omega_{ffv} = 1000 \times 2\pi$ rad/s. Figs. 12 and 13 show the Nyquist diagrams of $T_{m.B7.p}(s)$ and $T_{m.B7.n}(s)$ in the full frequency range $(-\infty, +\infty)$ and in the positive frequency range $(0, +\infty)$, respectively. As mentioned in Section II-C1, the Nyquist diagrams of both $T_{m.B7.p}(s)$ and $T_{m.B7.n}(s)$ are approximately symmetrical in the full frequency range $(-\infty, +\infty)$. Fig. 14 shows the pole-zero maps of $T_{m.B7.p}(s)$ and $T_{m.B7.n}(s)$, respectively. There is zero encirclement of the point $(-1, j0)$ in both cases, but there are two RHP poles in Case 2. Therefore, the system is stable in Case 1, but unstable in Case 2. The same stability results can be obtained from the pole-zero maps of $T_{clm.B7.p}(s)$ and $T_{clm.B7.n}(s)$, as shown in Fig. 15.

As shown above, the existing impedance-based Nyquist stability criterion is a necessary and sufficient condition, but it requires the examination of the RHP poles of the impedance ratio, which may need large computation effort for complicated systems or even cannot be obtained when detailed models of

TABLE VI
TYPES OF COMPONENT CONNECTIONS

Connection Type	Example	Stability criterion	Equivalent impedance or admittance	Terminal characteristic of the subsystem
Type 1	Fig. 16(a)	Naturally stable	$Y_{eqc} = Y_l + Y_{oc1} + Y_{oc2} + Y_{sysc1}$	Y-type (see Fig. 16(c))
Type 2	Fig. 16(b)	The impedance ratio $T_m = Y_{oc1} Z_l$ meets the Nyquist stability criterion.	$Y_{eqc} = \frac{Y_{oc1}}{1 + Y_{oc1} Z_l}$	Y-type (see Fig. 16(c))
Type 3	Fig. 17(a)	Naturally stable	$Z_{eqv} = Z_l + Z_{ov1}$	Z-type (see Fig. 17(d))
Type 4	Fig. 17(b)	The closed minor loop gain $T_{clm} = \frac{1}{1 + T_m} = \frac{Z_{sysv1}}{Z_{ov1} + Z_{sysv1}}$ meets the impedance-sum-type criterion [34].	$Z_{eqv} = \frac{Z_{ov1} Z_{sysv1}}{Z_{ov1} + Z_{sysv1}}$	Z-type (see Fig. 17(d))
Type 5	Fig. 17(c)	The impedance ratio $T_m = Y_{sysc1} Z_{ov1}$ meets the Nyquist stability criterion.	$Z_{eqv} = \frac{Z_{ov1}}{1 + Y_{sysc1} Z_{ov1}}$	Z-type (see Fig. 17(d))
Meshed	Section III-E	The proposed Method 2 in Section III-D	N.A.	N.A.

inverters are not available. The latter may cause trouble to system integrators for system stability assessment [13].

C. Proposed Stability Analysis Method 1: Using Stability Criteria Multiple Times in Succession

Clearly, it is desirable to avoid the examination of the RHP poles of the impedance ratios, for inverter-based multibus ac systems with both voltage-controlled and current-controlled inverters. The first proposed method is to add the system components one by one from nodes in the lowest level to areas in the highest system level, and accordingly, apply the stability criteria multiple times in succession, and the system is stable if all the stability check results indicate stability.

The terminal characteristics of system components can be classified into two types: impedance (Z) type and admittance (Y) type [34], [51], [52]. Passive components can be considered as Z-type in series connections and Y-type in parallel or meshed connections. The terminal characteristics of current-controlled inverters and voltage-controlled inverters can be regarded as Y-type and Z-type without RHP poles, respectively, when the current and voltage control loops are designed as stable.

Except mesh-type connections, the majority of the connections among these passive and active components in inverter-based ac systems can be categorized into the following groups. *Type 1*: Y+Y parallel-type connection [10], [13], [31], [33]. *Type 2*: Y+Z series-type connection [19], [22], [33]. *Type 3*: Z+Z series-type connection [35]. *Type 4*: Z+Z parallel-type connection [34], [35]. *Type 5*: Z+Y parallel-type connection [14], [25], [26], [32]. The stability criteria and total equivalent terminal characteristics of all the connection types are summarized in Table VI.

Type 4 connection needs to meet the impedance-sum-type criterion [34] based on Cauchy's theorem (or the principle of argument) [53], as shown in (17)–(19), where $N_{(0,j_0)}()$ is the number of times that the Nyquist trajectory encircles the critical point $(0, j_0)$ in an anticlockwise direction. Type 4 connection is stable if and only if $Z(1 + T_m)$ or $Z(Z_{ov1} + Z_{sysv1})$ is zero. The direct application of Cauchy's theorem on (18) is equivalent to the application of Nyquist stability criterion on T_m , which means that the RHP poles of the impedance ratio T_m still need

to be checked. However, the application of Cauchy's theorem on (19) avoids the RHP pole calculation because $P(Z_{ov1} + Z_{sysv1})$ is 0

$$T_m = \frac{Z_{ov1}}{Z_{sysv1}}, \quad T_{clm} = \frac{1}{1 + T_m} = \frac{Z_{sysv1}}{Z_{ov1} + Z_{sysv1}} \quad (17)$$

$$Z(1 + T_m) = P(1 + T_m) - N_{(0,j_0)}(1 + T_m) \quad (18)$$

$$Z(Z_{ov1} + Z_{sysv1}) = P(Z_{ov1} + Z_{sysv1}) - N_{(0,j_0)}(Z_{ov1} + Z_{sysv1}). \quad (19)$$

The harmonic stability of meshed-type connections can be analyzed by using the proposed Method 2 which will be described in Section III-D to avoid the RHP pole calculation of impedance ratios and one example will be given in Section III-E.

Based on the aforementioned summary of all the connection types, the analysis procedure of the proposed Method 1 can be illustrated in Fig. 18. The analysis is conducted from the lowest level (Level 1) to the highest level (system level). The sequence of adding components on each level is from the farthest terminal to the connection point with the higher level, and the harmonic stability of system-level meshed interconnections can be analyzed by the proposed Method 2 that will be presented in Section III-D. It should be mentioned that the subsystem assembled in the previous step should be stable before adding the next component. Therefore, the proposed Method 1 is conservative. There is a possibility that the addition of the next component can stabilize an unstable subsystem assembled in the previous step. However, such case can be avoided by the proposed Method 1.

The two-area system under study can be partitioned and re-assembled in five steps, and correspondingly, the system harmonic stability can be assessed by five successive stability checks, as illustrated in Fig. 19. For conciseness, only the stability analysis results in the positive-sequence domain are presented here. Fig. 20 shows the Bode plot and Nyquist diagram of the denominator $D_{clm_C1-p}(s)$ of the closed minor loop gain $T_{clm_C1-p}(s)$ as expressed in (20) for Check #1 at Bus 6 in both Case 1 and Case 2. It can be observed that as the frequency ω goes to the infinity, the magnitude of $D_{clm_C1-p}(s)$ goes to the infinity while the phase angle remains around 90° . That is because the order of the numerator $D_{clm_C1-p}^{\text{Num}}(s)$ of $D_{clm_C1-p}(s)$

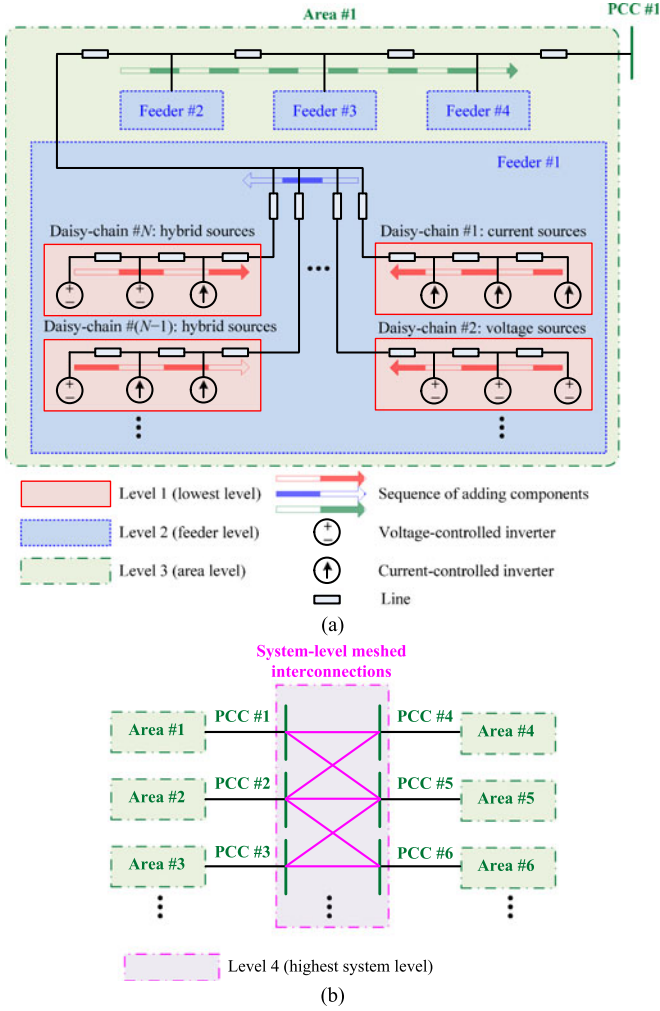


Fig. 18. Illustration of analysis procedure for a general inverter-based multi-area system: (a) within one area and (b) system level.

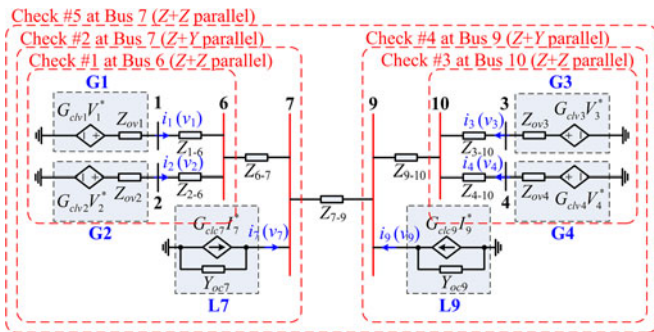


Fig. 19. Stability analysis of the two-area system by five stability checks in succession.

as defined in (21) is one order higher than that of the denominator $D_{clm_C1-p}^{Den}(s)$. For sequence admittances $Y_{oci-p}(s)$ ($i = 7, 9$) of current-controlled inverters, the order difference between the numerator and the denominator is -1 , as seen from the -90° phase in the high-frequency range in Fig. 4. Similarly, the order difference is 1 for sequence impedance $Z_{ovj-p}(s)$ ($j = 1 - 4$)

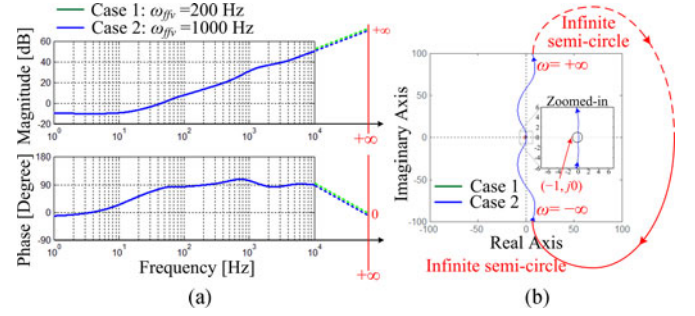


Fig. 20. (a) Bode plot and (b) Nyquist diagram of the denominator $D_{clm_C1-p}(s)$ in Case 1 and Case 2.

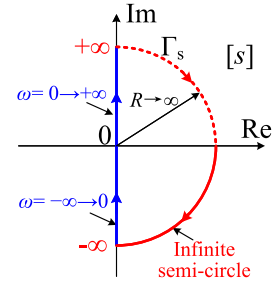


Fig. 21. Nyquist contour Γ_s in the s -plane.

of voltage-controlled inverters, as observed in Fig. 6, and the order difference is 1 for the inductive line impedance $Z_{lk-p}(s)$

$$T_{clm_C1-p}(s) = \frac{N_{clm_C1-p}(s)}{D_{clm_C1-p}(s)} = \frac{Z_{ov2-p}(s) + Z_{2-6-p}(s)}{Z_{ov1-p}(s) + Z_{1-6-p}(s) + Z_{ov2-p}(s) + Z_{2-6-p}(s)} \quad (20)$$

$$D_{clm_C1-p}(s) = \frac{D_{clm_C1-p}^{Num}(s)}{D_{clm_C1-p}^{Den}(s)}. \quad (21)$$

When drawing the Nyquist plot, the Nyquist trajectory segment corresponding to the infinite semicircle in clockwise direction of the Nyquist contour Γ_s in the s -plane ($[s]$), as shown in Fig. 21, should also be considered. When the numerator order is higher than the denominator order, such Nyquist trajectory segment is also an infinite semicircle in clockwise direction in the Nyquist complex plane, as illustrated in Fig. 20(b) and also presented as dash lines with phase angle changes of -90° between $\omega = 10^4 \times 2\pi$ rad/s and $\omega = +\infty$ in the Bode plot in Fig. 20(a) to assist the explanation. By examining the positive frequency range of the Bode plot, 180° increase in the phase angle means encircling the $(0, j0)$ point once in anti-clockwise direction, while 180° decrease in the phase angle means encircling the $(0, j0)$ point once in clockwise direction. According to the Bode plot of $D_{clm_C1-p}(s)$ in Fig. 20(a), $N_{(0,j0)}(D_{clm_C1-p}(s)) = 0$, and, thus, $Z(D_{clm_C1-p}(s)) = 0$ based on Cauchy's theorem. Therefore, the connection at Bus 6 for Check #1 is stable in both Case 1 and Case 2 in the positive-sequence domain.

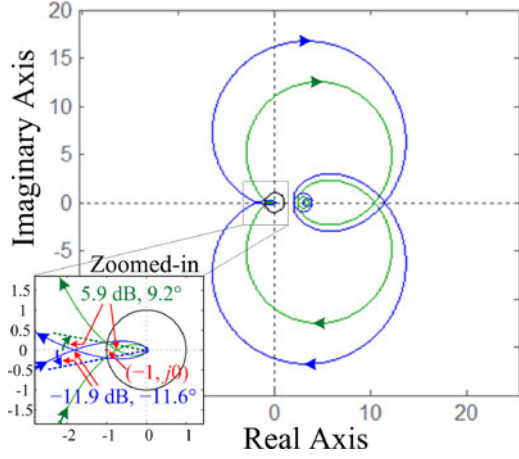


Fig. 22. Nyquist diagram of the impedance ratio $T_{m,C2,p}(s)$ in Case 1 and Case 2.

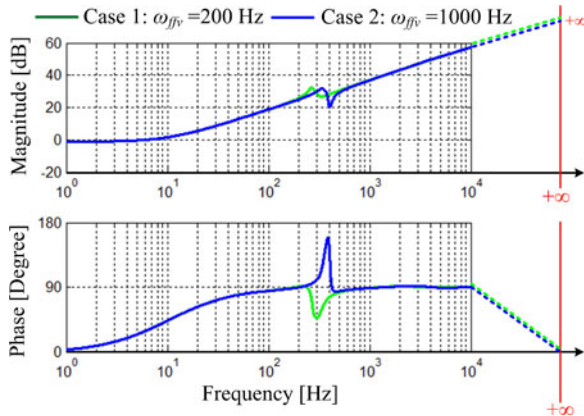


Fig. 23. Bode plot of the denominator $D_{clm,C5,p}(s)$ in Case 1 and Case 2.

Fig. 22 shows the Nyquist diagram of the impedance ratio $T_{m,C2,p}(s)$ for Check #2 at Bus 7 in the two cases. The trajectory in Case 1 does not encircle the point $(-1, j0)$ but the trajectory in Case 2 encircles the point $(-1, j0)$ twice in the clockwise direction. Therefore, the connection at Bus 7 for Check #2 is stable in Case 1 but unstable in Case 2 in the positive-sequence domain. According to the Nyquist trajectories, the gain margin is 5.9 dB and phase margin is 9.2° in Case 1, while the gain margin is -11.9 dB and phase margin is -11.6° in Case 2. Similar to Area 1, the Area 2 subsystem is stable in Case 1 but unstable in Case 2. Bode plot of the denominator $D_{clm,C5,p}(s)$ of the closed minor loop gain $T_{clm,C5,p}(s)$ for Check #5 at Bus 7 has zero encirclement around the point $(0, j0)$ in both cases, as shown in Fig. 23. Therefore, the total two-area system is stable in Case 1 but unstable in Case 2.

The calculation of the RHP poles of impedance ratios is avoided in the proposed Method 1, which reduces the computation burden as compared to the existing method using the Nyquist criterion once. However, the proposed Method 1 is conservative, due to the requirement that the subsystem for every

stability check should be stable, and the multistep process could be tedious for complicated systems.

The novelty of the proposed Method 1 is summarized as follows, as compared with the regional impedance-based stability analysis method presented in [33].

- 1) Although the stability analysis of the major connection types have been discussed individually in the existing literature, the proposed Method 1 systematically summarizes the stability criteria and total equivalent terminal characteristics of major connection types in the aspect of interconnection among components and subsystems, in order to facilitate the system-level harmonic stability analysis in a sequential manner. In addition, the stability criterion of meshed-type connections without the need for RHP pole calculation is proposed.
- 2) A sequential procedure of applying the existing criteria for major connection types and the proposed criterion for meshed connections to the harmonic stability analysis of general inverter-based multiarea ac systems is proposed to avoid the RHP pole calculation.
- 3) While Yoon *et al.* [33] only considered the radial distributed power systems consisting of only passive components and current-controlled inverters, the proposed Method 1 considers a general ac system composed of both current-controlled and voltage-controlled inverters.
- 4) The regional analysis method in [33] only dealt with Type 1 and Type 2 connections, while the proposed Method 1 is applicable to any ac system structures made up of all the major connection types and meshed connections.

D. Proposed Stability Analysis Method 2: Using Proposed Stability Criterion Based on Cauchy's Theorem Once

The impedance-sum-type criterion proposed in [34] is based on Cauchy's theorem and it can avoid the RHP pole calculation of impedance ratios. However, it is only applicable to systems with Type 4 (Z+Z parallel type) connection. Liu *et al.* [34] further considered applying Cauchy's theorem to the stability analysis of single-bus systems, in which both voltage-controlled and current-controlled converters are directly connected to the common bus in parallel [54], [55]. However, the derived two-step stability criterion is not an extension of the impedance-sum-type criterion. In addition, the application of Cauchy's theorem to a multibus general ac system with both voltage-controlled and current-controlled inverters and complicated connections including mesh has not been reported in the existing literature yet, and the underlying principle of the impedance-based stability analysis using Cauchy's theorem has not been clearly described yet. This paper fills in the gap by clearly identifying the underlying principle and generally extending the impedance-sum-type criterion for the harmonic stability analysis of any inverter-based multibus ac systems.

An impedance-based stability criterion is proposed here to assess the harmonic stability of inverter-based multibus ac systems without the need for the RHP pole calculation of the impedance ratios, and it only needs one stability examination and the consequent stability condition is necessary and sufficient.

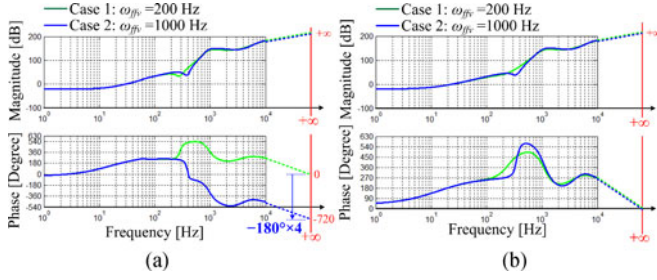


Fig. 24. Bode plots of denominators in the modified form in Case 1 and Case 2: (a) $D_{clm_B7_p}(s)$ and (b) $D_{clm_B7_n}(s)$.

The closed minor loop gain T_{clm_B7} can be rearranged to the form in

$$T_{clm_B7} = \frac{N_{clm_B7}(Y_{oci}, Z_{ovj}, Z_{lk})}{D_{clm_B7}(Y_{oci}, Z_{ovj}, Z_{lk})} \quad (22)$$

where the numerator N_{clm_B7} and the denominator D_{clm_B7} in the modified form are functions of the impedances or admittances of all individual components, including the admittances of current-controlled inverters Y_{oci} ($i = 7, 9$), the impedances of voltage-controlled inverters Z_{ovj} ($j = 1 - 4$), and the line impedances Z_{lk} . More importantly, these functions only involve multiplication and addition operations.

The underlying principle of the impedance-based stability analysis using Cauchy's theorem is explained as follows. Because each inverter is designed to operate stably alone, Y_{oci} and Z_{ovj} are all stable without RHP poles. The line impedances Z_{lk} are passive, and, thus, stable without RHP poles. Since the multiplication and addition operations do not introduce additional RHP poles, both N_{clm_B7} and D_{clm_B7} have zero RHP poles. Therefore, the system stability is determined by the RHP zeros of D_{clm_B7} , which can be estimated by (23) based on Cauchy's theorem. The system is stable if and only if $N_{(0,j0)}(D_{clm_B7})$ is zero. By using the modified form of T_{clm_B7} for stability analysis, the RHP pole calculation is avoided

$$\begin{aligned} Z(D_{clm_B7}) &= P(D_{clm_B7}) - N_{(0,j0)}(D_{clm_B7}) \\ &= -N_{(0,j0)}(D_{clm_B7}). \end{aligned} \quad (23)$$

The previous two cases are analyzed again using the proposed stability criterion. Fig. 24 displays the Bode plots of the denominators D_{clm_B7} in the modified form in Case 1 and Case 2 in both the positive-sequence domain $D_{clm_B7_p}(s)$ and the negative-sequence domain $D_{clm_B7_n}(s)$. The phase angles of $D_{clm_B7_p}(s)$ in Case 1 remain around 270° when the frequency is high, because the order of the numerator $D_{clm_B7_p}^{Num}(s)$ of $D_{clm_B7_p}(s)$ is higher than the order of the denominator $D_{clm_B7_p}^{Den}(s)$, and the order difference is 3. The same goes for $D_{clm_B7_n}(s)$ in the negative-sequence domain. Considering the infinite semicircle segments of Nyquist trajectories, the phase angles decrease by $90^\circ \times 3 = 270^\circ$ from $\omega = 10^4 \times 2\pi$ rad/s to $\omega = +\infty$ in Fig. 24.

According to the Bode plots of $D_{clm_B7_p}(s)$ in Fig. 24(a), the overall net phase variations in the frequency range of $[0, +\infty)$ are 0° in Case 1 but $-180^\circ \times 4 = -720^\circ$ in Case 2. It means that

$N_{(0,j0)}(D_{clm_B7_p}(s)) = 0$, and, thus, $Z(D_{clm_B7_p}(s)) = 0$ in Case 1, while $N_{(0,j0)}(D_{clm_B7_p}(s)) = -4$, and, thus, $Z(D_{clm_B7_p}(s)) = 4$ in Case 2. As for the Bode plots of $D_{clm_B7_n}(s)$ in Fig. 24(b), $N_{(0,j0)}(D_{clm_B7_n}(s)) = 0$, and, thus, $Z(D_{clm_B7_n}(s)) = 0$ in both Case 1 and Case 2. Therefore, the multibus ac system under study is stable in Case 1, while it is unstable in Case 2 and the instability occurs in the positive-sequence system.

In summary, the proposed stability criterion based on Cauchy's theorem can be described as follows.

- Step 1:* Get the frequency responses of stable sequence admittances Y_i or impedances Z_j of all components in the system, which can be obtained by impedance measurement, or from the Bode plots of the transfer functions of the sequence admittances or impedances. Determine the order difference between the numerator and the denominator of each Y_i or Z_j .
- Step 2:* Divide the total system into two subsystems at any bus, and derive the expression of the closed-loop gain T_{clm} of the impedance ratio T_m as functions of Y_i and Z_j .
- Step 3:* Change the form of T_{clm} into $T_{clm} = N_{clm} / D_{clm}$, where N_{clm} and D_{clm} are functions of Y_i and Z_j with only multiplication and addition operations.
- Step 4:* Check the order difference between the numerator and denominator of D_{clm} , by examining each summation term in D_{clm} , in order to determine the phase angle change of D_{clm} corresponding to the infinite semicircle segments of Nyquist trajectories.
- Step 5:* Draw the Nyquist or Bode plots of D_{clm} and count the encirclement of the point $(0, j0)$ in anticlockwise direction $N_{(0,j0)}(D_{clm})$. The system is stable if and only if $N_{(0,j0)}(D_{clm})$ is zero.

The above steps should be executed in both the positive-sequence domain and the negative-sequence domain. The proposed stability criterion is a necessary and sufficient condition and the RHP poles calculation is avoided, which reduces the computation effort and enables the stability assessment when the component impedances can only be measured. It is worth noting that the reformation in Step 3 can be done in MATLAB using the "collect" command for symbolic expressions.

The novelty of the proposed Method 2 is summarized as follows.

- 1) The underlying principle of the impedance-based stability analysis using Cauchy's theorem is clearly identified. Reformed closed minor loop gains with only multiplication and addition operations can avoid the RHP pole calculation.
- 2) While the existing impedance-sum-type criterion is only applicable to single-bus systems with Type 4 ($Z+Z$ parallel type) connection, the proposed Method 2 generally extends the application of Cauchy's theorem to the harmonic stability analysis of any multibus ac systems with any structures including all the major connection types and meshed connections.
- 3) The approach of using Bode plots in the positive frequency range instead of Nyquist diagrams to determine

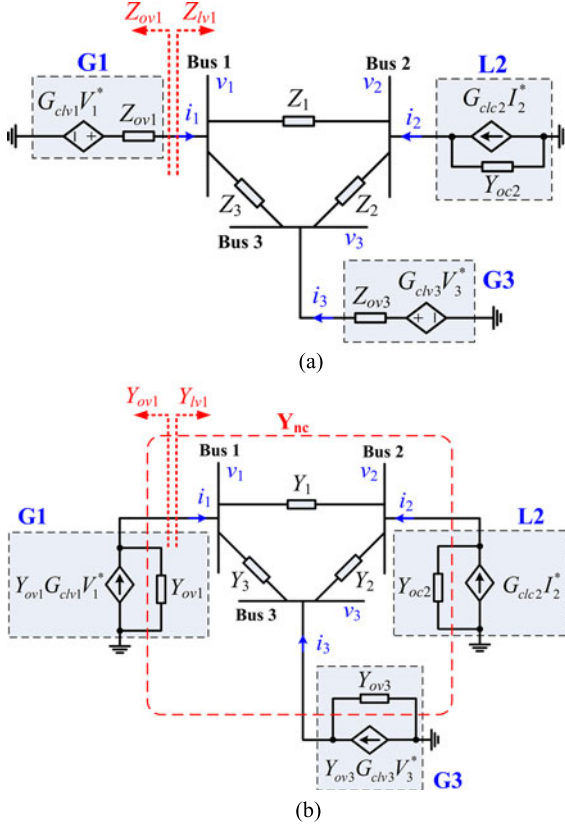


Fig. 25. Impedance-based circuits of the meshed system: (a) Original circuit and (b) equivalent Norton circuit.

the encirclement of the origin point $(0, j0)$ is demonstrated. Specifically, it is emphasized that it is necessary to check the order difference between the numerator and denominator of a transfer function, in order to determine the phase angle change corresponding to the infinite semi-circle segments of Nyquist trajectories, when drawing the Bode plots.

E. Application of the Proposed Method 2 to Meshed Systems

In order to demonstrate the effectiveness of the proposed Method 2 in the harmonic stability analysis of meshed systems, one three-bus meshed system is configured with two voltage-controlled inverters G1 and G3 and one current-controlled inverter L2 connected to Bus 1, Bus 3, and Bus 2, respectively, as shown in Fig. 25(a). The inverter parameters are the same as those listed in Tables I–III, except the values of ω_{ffv} in Case 11 ($\omega_{ffv} = 200 \times 2\pi$ rad/s) and Case 12 ($\omega_{ffv} = 1000 \times 2\pi$ rad/s). The impedances of three lines are $Z_1 = Z_{1-6}$, $Z_2 = Z_{2-6}$, and $Z_3 = Z_{6-7}$, respectively, where Z_{1-6} , Z_{2-6} , and Z_{6-7} are given in Table IV. The operating point of the meshed system is the same as that listed in Table V.

The application of the proposed Method 2 is described as follows. For conciseness, only the harmonic stability analysis in the positive-sequence domain is presented.

Step 1: The sequence impedances Z_{ov1} and Z_{ov3} of G1 and G3 and the sequence admittance Y_{oc2} of L2 are described in

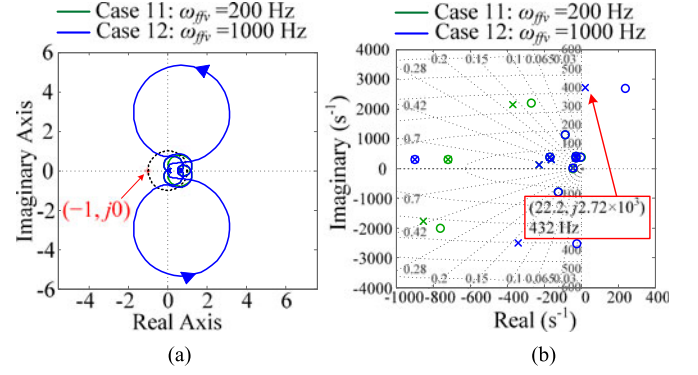


Fig. 26. (a) Nyquist diagrams and (b) pole-zero maps of the positive-sequence impedance ratios $T_{m.B1.p}(s)$ at Bus 1 of the meshed system in Case 11 and Case 12.

Section II. The sequence impedances of lines are presented in Section III-B.

Step 2: The meshed system is divided into two subsystems with impedances Z_{ov1} and Z_{lv1} , respectively, at Bus 1. The impedance ratio $T_{m.B1}$ and the closed minor loop gain $T_{clm.B1}$ at Bus 1 are expressed in (24) and (25), which can be derived based on the method developed in [9]:

$$T_{m.B1} = \frac{Z_{ov1}}{Z_{lv1}} = \frac{1}{T_{clm.B1}} - 1 \quad (24)$$

$$T_{clm.B1} = \frac{1}{1 + T_{m.B1}} = \frac{1}{1 + \frac{Z_{ov1}}{Z_{lv1}}}. \quad (25)$$

By replacing the Thevenin models of G1 and G3 with their equivalent Norton models, the system impedance-based circuit is depicted in Fig. 25(b) with some variables defined as

$$Y_{ov1} = \frac{1}{Z_{ov1}}, Y_{ov3} = \frac{1}{Z_{ov3}} \quad (26)$$

$$Y_1 = \frac{1}{Z_1}, Y_2 = \frac{1}{Z_2}, Y_3 = \frac{1}{Z_3}, Y_{lv1} = \frac{1}{Z_{lv1}}. \quad (27)$$

Based on the system nodal admittance matrix Y_{nc} , $T_{clm.B1}$ can be obtained as (28), where Y_{nom} is expressed in (29). Then, $T_{m.B1}$ can be derived by substituting (28) into (24):

$$T_{clm.B1} = \frac{Y_{ov1} \begin{bmatrix} Y_1 Y_2 + Y_1 Y_3 + Y_2 Y_3 \\ + (Y_2 + Y_3) Y_{oc2} + (Y_1 + Y_2 + Y_{oc2}) Y_{ov3} \end{bmatrix}}{Y_{nom}} \quad (28)$$

$$Y_{nom} = (Y_1 Y_2 + Y_1 Y_3 + Y_2 Y_3) (Y_{ov1} + Y_{ov3} + Y_{oc2}) \\ + (Y_1 + Y_2 + Y_{oc2}) Y_{ov1} Y_{ov3} + \left[(Y_2 + Y_3) Y_{ov1} \right. \\ \left. + (Y_1 + Y_3) Y_{ov3} \right] Y_{oc2}. \quad (29)$$

As illustrated in Fig. 26, although the Nyquist plot of the positive-sequence impedance ratio $T_{m.B1.p}(s)$ has zero encirclement of the critical point $(-1, j0)$ in both cases, one RHP pole exists in Case 12. It should be noted that another conjugate RHP

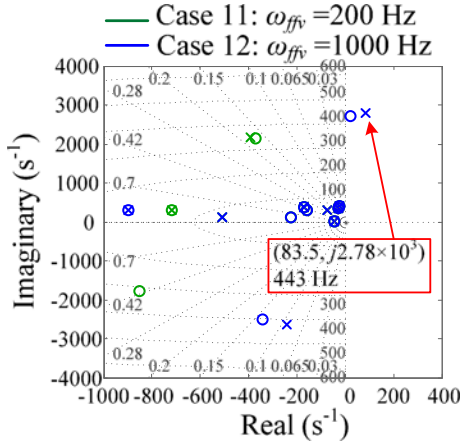


Fig. 27. Pole-zero maps of the closed-loop gains $T_{clm_B1-p}(s)$ of the positive-sequence impedance ratios at Bus 1 of the meshed system in Case 11 and Case 12.

pole exists in the negative-sequence domain in Case 12. Therefore, the meshed system is stable in Case 11 but unstable in Case 12. According to the pole-zero maps of the positive-sequence closed minor loop gain $T_{clm_B1-p}(s)$, as shown in Fig. 27, the unstable frequency of the system RHP pole in Case 12 is 443 Hz in the positive-sequence domain.

Step 3: After substituting (26) into (28), the closed minor loop gain T_{clm_B1} is reformatted as (30), with the numerator N_{clm_B1} and the denominator D_{clm_B1} in the modified forms as expressed in (31) and (32):

$$T_{clm_B1} = \frac{N_{clm_B1}}{D_{clm_B1}} \quad (30)$$

$$N_{clm_B1} = Y_1 + Y_2 + Y_{oc2} + (Y_1 Y_2 + Y_1 Y_3 + Y_2 Y_3) Z_{ov3} + (Y_2 + Y_3) Y_{oc2} Z_{ov3} \quad (31)$$

$$D_{clm_B1} = Y_1 + Y_2 + Y_{oc2} + \left(Y_1 Y_2 + Y_1 Y_3 + Y_2 Y_3 \right) \left(Z_{ov1} + Z_{ov3} + Y_{oc2} Z_{ov1} Z_{ov3} \right) + \left[\left(Y_1 + Y_3 \right) Z_{ov1} + \left(Y_2 + Y_3 \right) Z_{ov3} \right] Y_{oc2}. \quad (32)$$

Step 4: There is one more Y-type variable than Z-type variables in each summation term in D_{clm_B1} . Therefore, the order difference between the numerator and the denominator of $D_{clm_B1}(s)$ is -1 , and the phase angle change of $D_{clm_B1}(s)$ is an increment of 90° , corresponding to the infinite semicircle segments of Nyquist trajectories.

Step 5: According to the Bode plots of the positive-sequence denominator $D_{clm_B1-p}(s)$ of $T_{clm_B1-p}(s)$, as illustrated in Fig. 28, the overall net phase variations in the frequency range of $[0, +\infty)$ are 0° in Case 11 but $-180^\circ \times 2 = -360^\circ$ in Case 12. It indicates that $N_{(0,j0)}(D_{clm_B1-p}(s))$ is 0 in Case

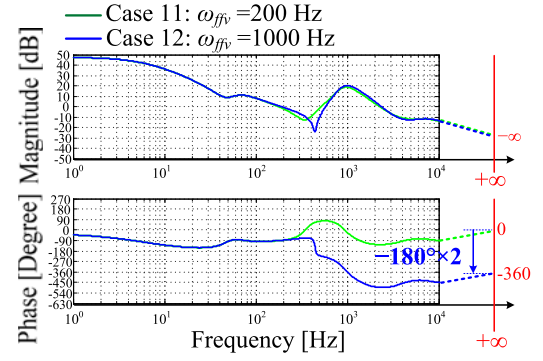


Fig. 28. Bode plots of the positive-sequence denominators $D_{clm_B1-p}(s)$ in the modified form in Case 11 and Case 12.

11 but -2 in Case 12, and the meshed system is stable in Case 11 but unstable in Case 12 with two RHP poles.

The aforementioned analysis shows that the proposed Method 2 can correctly analyze the harmonic stability of meshed systems without the need for the RHP pole calculation of the impedance ratios. The experimental verification will be presented in Section V-D.

F. Comparison of Harmonic Stability Analysis Methods

The aforementioned three methods for harmonic stability analysis of inverter-based multibus ac systems have been compared regarding 1) necessity and sufficiency, 2) requirement on impedance model details, 3) RHP pole calculation of the impedance ratio, 4) number of stability checks, 5) computation time, and 6) stability margins (gain margin and phase margin), as shown in Table VII. As compared with the existing method, the proposed Method 1 and Method 2 not only have less strict requirements on the impedance models, which enables the stability assessment using measured impedances, but also take significantly less computation time by avoiding formulating the transfer function of the impedance ratio and calculating the RHP poles of the impedance ratio.

IV. CONTROLLER PARAMETER DESIGN OF INVERTERS

A. Controller Parameter Design Process

For inverter-based multibus ac systems with multiple voltage-controlled and current-controlled inverters, it is not easy to design the controller parameters of each inverter individually because the system stability is determined by the interconnection of all inverters.

Before interconnecting all inverters to construct the system, each individual inverter should be designed to be stable internally (with ideal external conditions), and the parameter range for *internal stability* of each inverter can be obtained. The aforementioned harmonic stability analysis methods can be repetitively applied for all the parameter sets within the parameters ranges with *internal stability*, in order to obtain the stable regions, unstable regions, and stability boundaries in the parameter space for the multibus system stability or *external*

TABLE VII
COMPARISON OF DIFFERENT HARMONIC STABILITY ANALYSIS METHODS

	Existing method (using Nyquist stability criterion once)	Proposed Method 1 (using stability criteria multiple times in succession)	Proposed Method 2 (using proposed stability criterion based on Cauchy's theorem once)
Necessity and sufficiency	Necessary and sufficient	Sufficient	Necessary and sufficient
Requirement on impedance model details	Transfer function models of impedances, which require the detailed internal control information of inverters.	Frequency response data of impedances, which can be generated by the transfer function models or measured without the need for internal control details.	Frequency response data of impedances, which can be generated by the transfer function models or measured without the need for internal control details.
RHP pole calculation of the impedance ratio	Required	Avoided	Avoided
Number of stability checks	One	Multiple	One
Computation time*	169.0 s	6.5 s	2.5 s
Stability margins (gain margin and phase margin)	Can tell the stability margins if the Nyquist trajectory intersects the unit circle.	1) For stability checks using Nyquist criterion: Can tell the stability margins if the Nyquist trajectory intersects the unit circle. 2) For stability checks using Cauchy's theorem: Cannot tell the stability margins.	Cannot tell the stability margins.

*: Frequency response data: 10 000 logarithmically equally spaced points between 10^{-2} and 10^5 Hz. Computation time listed is an average value for computation of the two-area system using MATLAB and a second-generation Intel Core i7 quad-core CPU.

interconnection stability of all inverters. Considering that the existing method is time consuming, the proposed Method 1 and Method 2 can be used for this iteration-type design process. It is worth noting that although the proposed Method 2 cannot tell the traditional gain or phase margins, the achieved stability boundary in the parameter space can still tell the stability margin from a different aspect, that is, the distance from the stability boundary.

For simplicity, it is assumed that all voltage-controlled inverters have same controller parameters and all current-controlled inverters have same controller parameters in the two-area system, and the cutoff frequency ω_{ffv} of the voltage feedforward control and the current-loop bandwidth ω_c of all current-controlled inverters as well as the voltage loop bandwidth ω_v of all voltage-controlled inverters are chosen to be designed. The values of ω_c and ω_v are achieved by setting the PI controller parameters as

$$\begin{cases} K_{cp} = \omega_c L_f, & K_{ci} = 875 K_{cp} \\ K_{vp} = \omega_v \left(2T_s + \frac{1}{\omega_{ffv}} \right), & K_{vi} = \omega_v \end{cases} \quad (33)$$

According to the Bode plots of the stable open-loop gains of the current-controlled inverters $T_{c,p}(s)$ and the voltage-controlled inverters $T_{v,p}(s)$ in the positive-sequence domain, as shown in Fig. 29, the value of ω_c is confined in the range of $[100 \times 2\pi, 1000 \times 2\pi \text{ rad/s}]$ for *internal stability* of current-controlled inverters, and the value of ω_v is confined in the range of $[50 \times 2\pi, 500 \times 2\pi \text{ rad/s}]$ for *internal stability* of voltage-controlled inverters. Since ω_{ffv} only changes the sequence admittances but does not change the current-loop stability of current-controlled inverters, the value of ω_{ffv} is confined in the range of $[100 \times 2\pi, 1000 \times 2\pi \text{ rad/s}]$.

B. Design Results of the Two-Area System

The design results of the parameter pair $(\omega_{ffv} \text{ and } \omega_c)$ are presented in the 2-D maps in Figs. 30 and 31 with ω_v equal to $170 \times 2\pi \text{ rad/s}$. The design results of the parameter pair $(\omega_v \text{ and } \omega_c)$ are shown in Fig. 32(a) with ω_{ffv} equal to $100 \times 2\pi \text{ rad/s}$

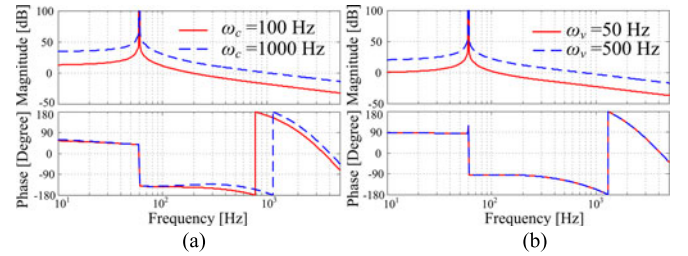


Fig. 29. Bode plots of the open-loop gains of (a) the current-controlled inverters $T_{c,p}(s)$ and (b) voltage-controlled inverters $T_{v,p}(s)$ in the positive-sequence domain.

and Fig. 32(b) with ω_{ffv} equal to $200 \times 2\pi \text{ rad/s}$. Since the system in the negative-sequence domain in the selected parameter space happens to be always stable, only the design results for the system in the positive-sequence domain are presented here.

Fig. 31 shows that the stability region generated using Method 1 (limited by Check #2) is relatively smaller than that generated using Method 2, which exhibits the conservativeness of Method 1. In addition, some general design rules for the studied two-area system can be derived. 1) The cutoff frequency ω_{ffv} of the voltage feedforward control cannot be very large. Larger ω_{ffv} makes the system more prone to instability. 2) The cutoff frequency ω_{ffv} of the voltage feedforward control should be smaller than the current-loop bandwidth ω_c . 3) The stability is mainly affected by the parameter ω_{ffv} instead of ω_v .

The stability boundaries obtained from the simulation results using MATLAB/Simulink are also shown in Fig. 30. The small but acceptable discrepancy between the analysis results and the simulation results near the stability boundaries is due to the limitation of the model accuracy described in Section II.

V. EXPERIMENTAL VERIFICATION

A. Experimental Setup

The experimental platform for scaled-down emulation of the two-area system using three-phase inverters and inductors has

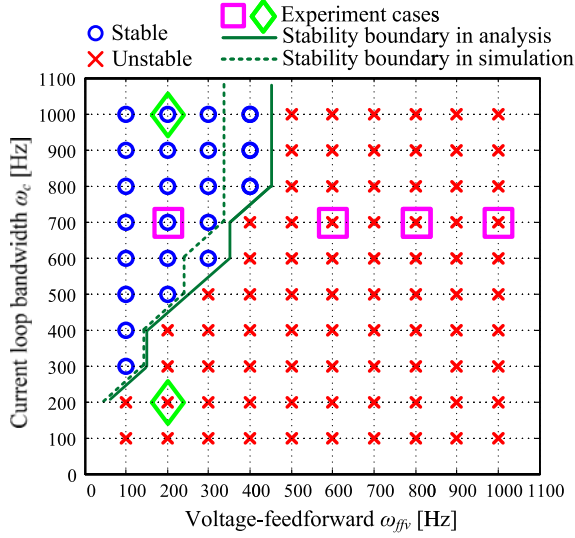


Fig. 30. Stability regions and stability boundaries in the map of the parameter pair (ω_{ffv} and ω_c) using the proposed Method 2.

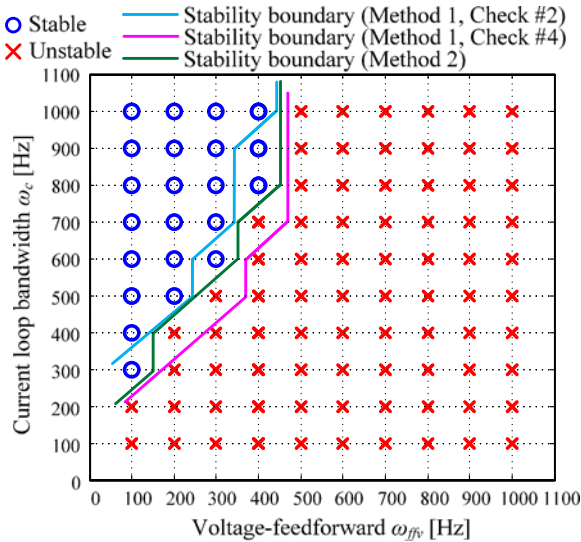
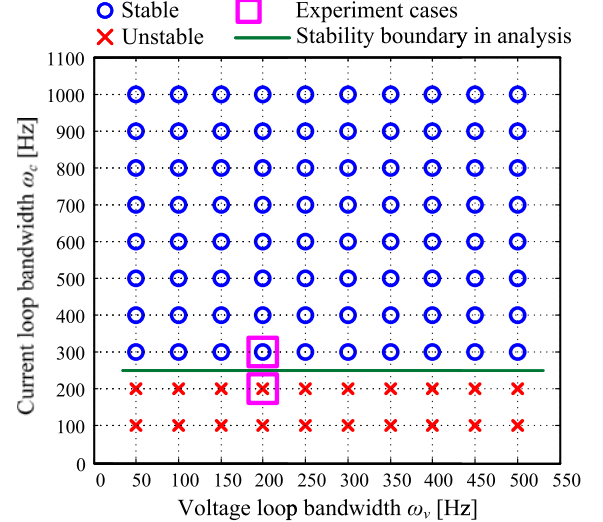


Fig. 31. Comparison of the stability boundaries generated using the proposed Method 1 and Method 2.

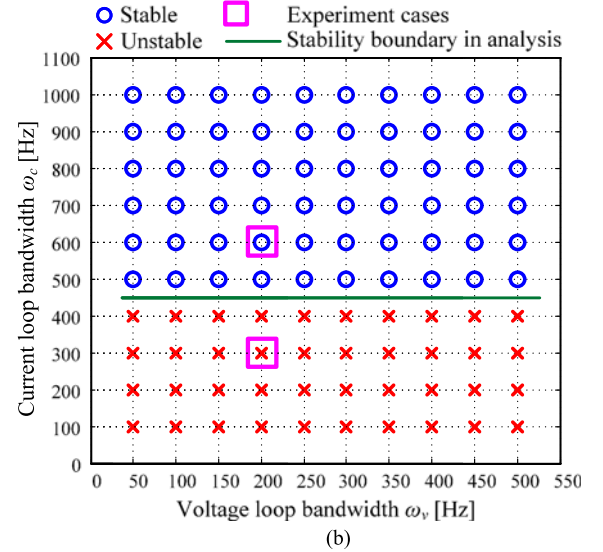
been set up, as shown in Fig. 33. The three-phase inverter as the emulator consists of the 75-kW power stage from Vacon company and a customized interface board with TMS320F28335 DSP of Texas Instruments. In the following experiments, the inverters run under a condition with power lower than manufacture power rating. The parameters of the inverters and inductors as well as the system operating points are the same as those listed in Tables I, IV, and V.

B. Design Verification of the Parameter Pair (ω_{ffv} and ω_c)

In order to verify the design results of the parameter pair (ω_{ffv} and ω_c) presented in the parameter map in Fig. 30, several experimental cases have been carried out, which are also marked as purple squares and green diamonds in Fig. 30.



(a)



(b)

Fig. 32. Stability regions and stability boundaries in the map of the parameter pair (ω_v and ω_c) using the proposed Method 2. (a) ω_{ffv} is $100 \times 2\pi$ rad/s and (b) ω_{ffv} is $200 \times 2\pi$ rad/s.

In the first case group (purple squares), ω_c is $700 \times 2\pi$ rad/s and ω_v is $170 \times 2\pi$ rad/s, while ω_{ffv} has four different values: $200 \times 2\pi$ (Case 1), $1000 \times 2\pi$ (Case 2), $800 \times 2\pi$ (Case 3), and $600 \times 2\pi$ rad/s (Case 4). Fig. 34 shows the experimental waveforms of the phase-A currents of G2, G4, L7, and L9 in the two-area system when ω_{ffv} changes from $200 \times 2\pi$ to $1000 \times 2\pi$ rad/s. It can be seen that the system changes from a stable state to an unstable state, which verifies the stability analysis in Section III. Fig. 35(a) and (b) displays the experimental results of the system in the unstable state when ω_{ffv} is $800 \times 2\pi$ and $600 \times 2\pi$ rad/s, respectively, which verifies the parameter design results shown in Fig. 30.

In the second case group (green diamonds), ω_v is $170 \times 2\pi$ rad/s and ω_{ffv} is $200 \times 2\pi$ rad/s, while ω_c has two different values: $1000 \times 2\pi$ (Case 5) and $200 \times 2\pi$ rad/s (Case 6). Fig. 36 illustrates the experimental results when ω_c changes from 1000

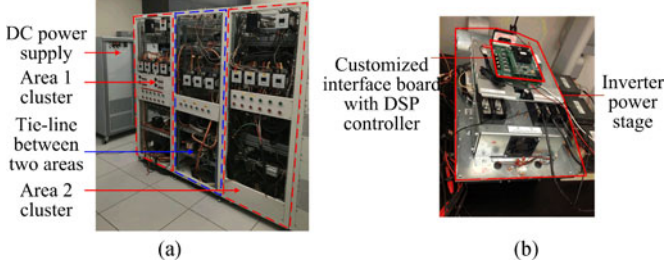


Fig. 33. Experimental setup of the inverter-based multibus ac system. (a) Photo of the total system. (b) Photo of the three-phase inverter.

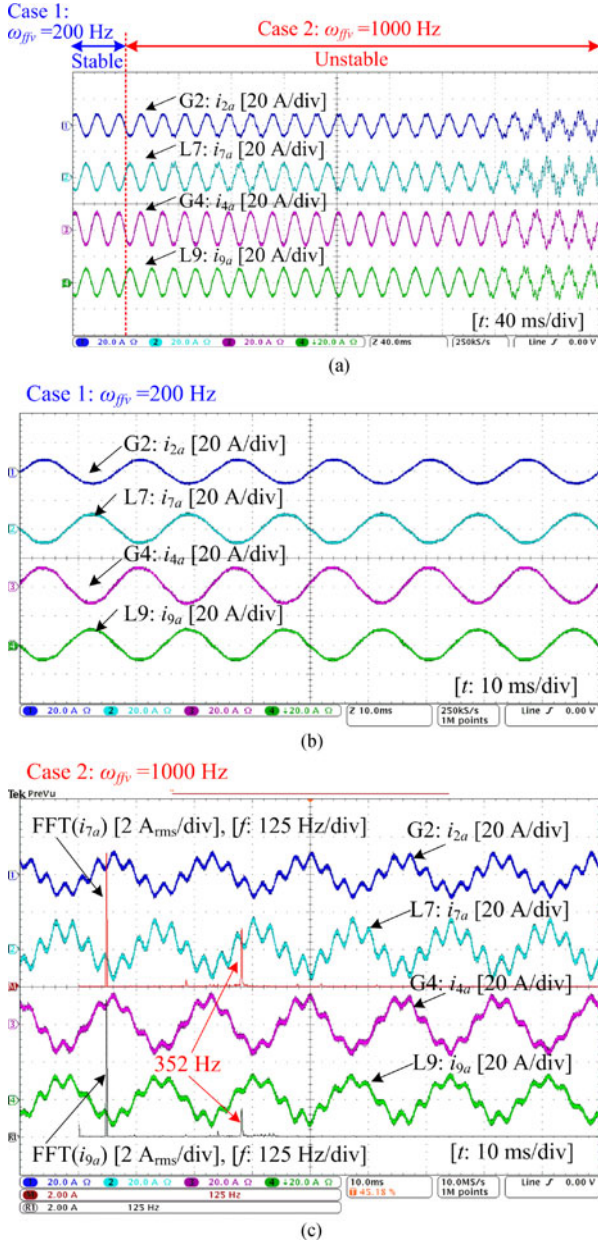


Fig. 34. Experimental results when ω_{ffv} changes from $200 \times 2\pi$ rad/s to $1000 \times 2\pi$ rad/s. (a) System transition from a stable state to an unstable state. (b) System in stable state when ω_{ffv} is $200 \times 2\pi$ rad/s. (c) System in unstable state when ω_{ffv} is $1000 \times 2\pi$ rad/s.

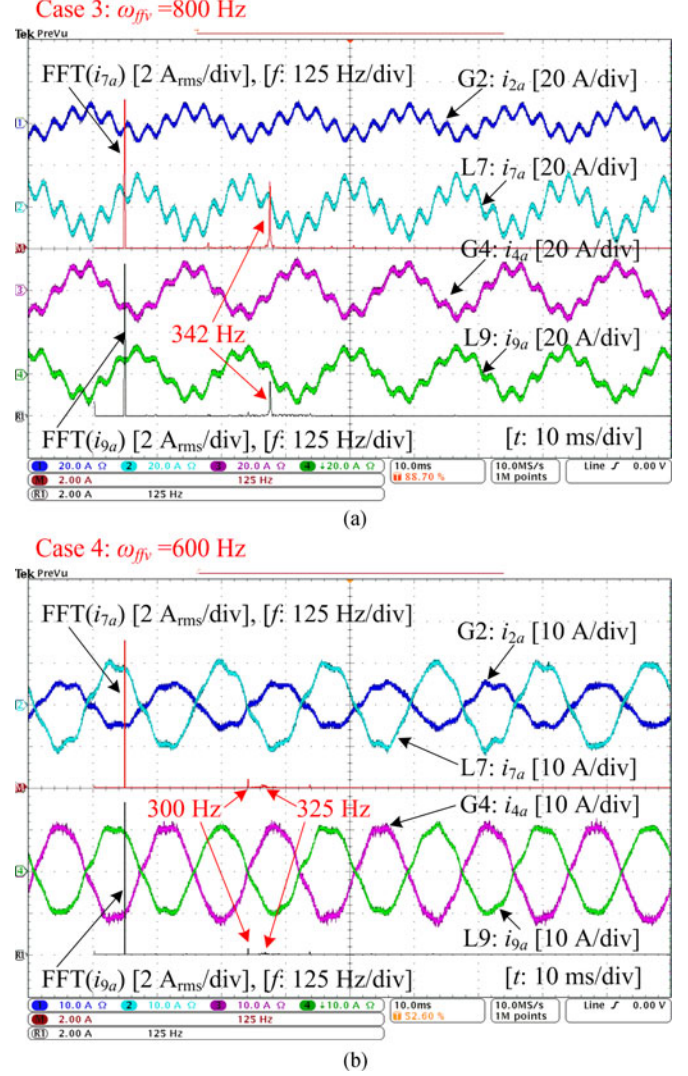


Fig. 35. Experimental results of the system in unstable state. (a) ω_{ffv} is $800 \times 2\pi$ rad/s. (b) ω_{ffv} is $600 \times 2\pi$ rad/s.

$\times 2\pi$ to $200 \times 2\pi$ rad/s. The system changes from a stable state to an unstable state, which verifies the parameter design results shown in Fig. 30.

C. Design Verification of the Parameter Pair (ω_v and ω_c)

Additional four experimental cases, marked as purple squares in Fig. 32, have been performed to verify the design results of the parameter pair (ω_v and ω_c) presented in the parameter maps in Fig. 32. In the first case group, ω_v is $200 \times 2\pi$ rad/s and ω_{ffv} is $100 \times 2\pi$ rad/s, while ω_c changes from $300 \times 2\pi$ (Case 7) to $200 \times 2\pi$ rad/s (Case 8). The experimental results presented in Fig. 37(a) show that the system changes from a stable state to an unstable state, which verifies the parameter design results shown in Fig. 32(a). In the second case group, ω_v is still $200 \times 2\pi$ rad/s, but ω_{ffv} is changed to $200 \times 2\pi$ rad/s, while ω_c changes from $600 \times 2\pi$ (Case 9) to $300 \times 2\pi$ rad/s (Case 10).

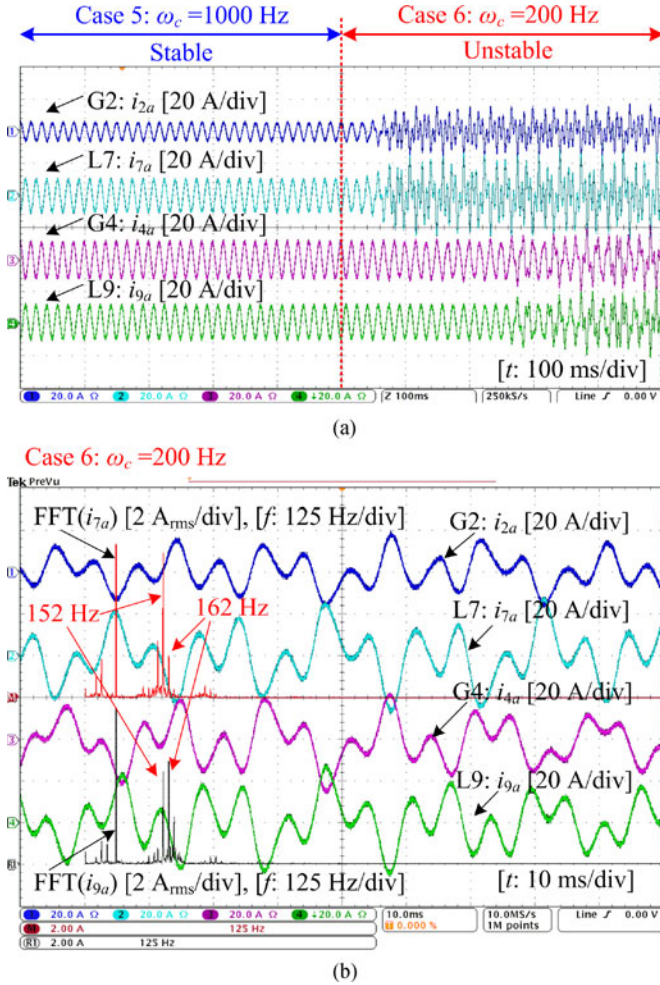


Fig. 36. Experimental results when ω_c changes from $1000 \times 2\pi$ rad/s to $200 \times 2\pi$ rad/s. (a) System transition from a stable state to an unstable state. (b) System in unstable state when ω_c is $200 \times 2\pi$ rad/s.

As illustrated in Fig. 37(b), the system changes from a stable state to an unstable state, which verifies the parameter design results shown in Fig. 32(b).

D. Verification of the Meshed System

The experimental platform has been reconfigured as the meshed system as depicted in Fig. 25. Case 11 and Case 12 have been verified in experiments. Fig. 38 shows the phase-A currents of inverters G1, G3, and L2 in the meshed system. It can be seen that the system changes from a stable state to an unstable state when the parameter ω_{ffv} changes from $200 \times 2\pi$ rad/s in Case 11 to $1000 \times 2\pi$ rad/s in Case 12.

E. Resonance Frequencies in Unstable Cases

When the system transits from a stable state to an unstable state, initially the dq currents have small diverging oscillations around the operating points. Then, similar to the phenomenon presented in [32], large diverging currents make the system reach the saturation state with restricted current oscillation magnitudes due to the saturation of controller outputs, so the

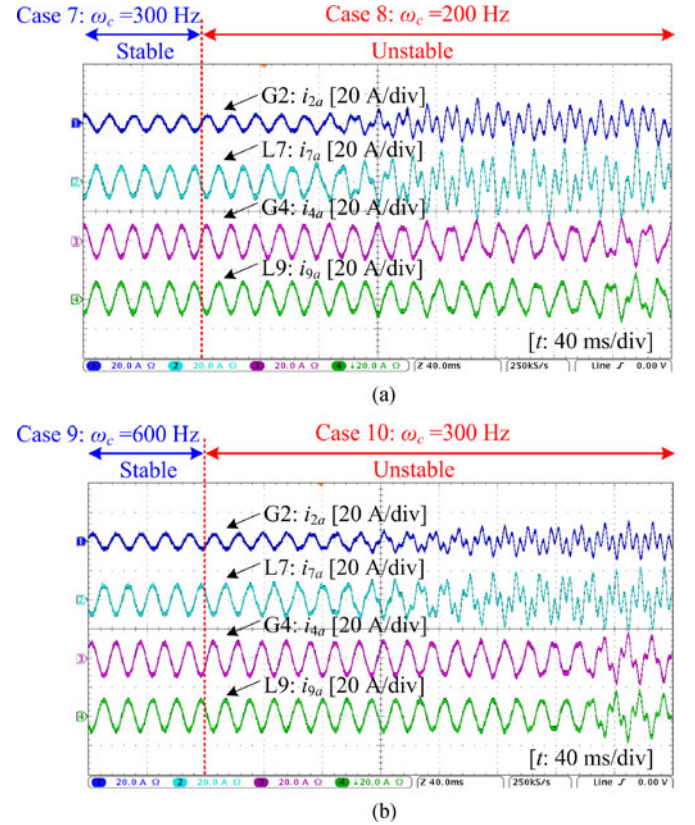


Fig. 37. Experimental results of system transition from a stable state to an unstable state: (a) ω_c changes from $300 \times 2\pi$ rad/s to $200 \times 2\pi$ rad/s, ω_v is $200 \times 2\pi$ rad/s and ω_{ffv} is $100 \times 2\pi$ rad/s and (b) ω_c changes from $600 \times 2\pi$ rad/s to $300 \times 2\pi$ rad/s, ω_v is $200 \times 2\pi$ rad/s and ω_{ffv} is $200 \times 2\pi$ rad/s.

TABLE VIII
RESONANCE FREQUENCIES IN UNSTABLE CASES

Case No.	Analysis	Major Resonances in Unstable Cases		
		In Initial States	In Saturation States	Saturation States
Case 2	366, 403 Hz	354 Hz	345, 364 Hz	352 Hz
Case 3	355, 391 Hz	343 Hz	338, 356 Hz	342 Hz
Case 4	340 Hz	340 Hz	326, 345 Hz	300, 325 Hz
Case 6	172, 183 Hz	171 Hz	169, 176 Hz	152, 162 Hz
Case 8	155 Hz	155 Hz	153 Hz	140 Hz
Case 10	197 Hz	197 Hz	195, 205 Hz	184 Hz
Case 12	443 Hz	420 Hz	405 Hz	420 Hz

resonance frequency could be slightly different from that in the aforementioned small-signal harmonic stability analysis.

The resonance frequencies in unstable cases are summarized in Table VIII. The differences between the major resonance frequencies in the initial states in simulation and the resonance frequencies in the analysis results are mostly within ± 15 Hz, while the differences between the major resonance frequencies in the saturation states in both simulation and experiments and the resonance frequencies in the analysis results are mostly within ± 25 Hz.

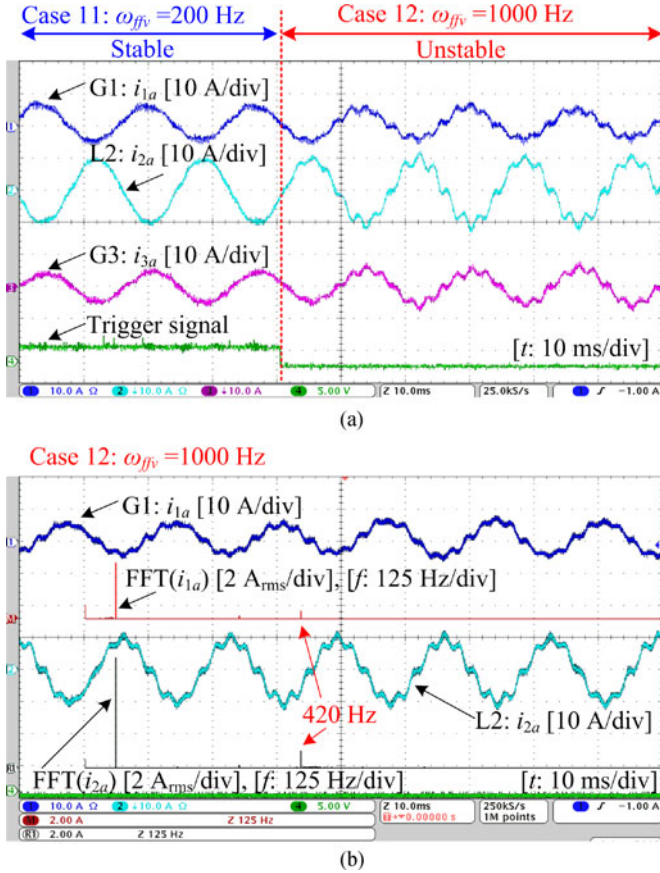


Fig. 38. Experimental results of the meshed system when ω_{ffv} changes from $200 \times 2\pi$ rad/s to $1000 \times 2\pi$ rad/s. (a) Transition from a stable state to an unstable state. (b) Unstable state when ω_{ffv} is $1000 \times 2\pi$ rad/s.

In summary, the experimental results have verified the stability analysis methods described in Section III and the controller parameter design results presented in Section IV.

VI. CONCLUSION

In this paper, two sequence-impedance-based methods for harmonic stability analysis of three-phase inverter-based multibus ac power systems have been proposed to avoid the examination of RHP poles of impedance ratios and reduce the computation effort, as compared with the existing stability analysis method using the Nyquist stability criterion once. The proposed methods also enable the system harmonic stability assessment using only measured sequence impedances of components, without the need for detailed internal control information of them.

The novelty of the proposed Method 1 is: 1) all the major connection types and the meshed connection are summarized, regarding the stability criteria and total equivalent terminal characteristics; 2) a sequential procedure of applying stability criteria to the harmonic stability analysis of general inverter-based multiarea ac systems is proposed to avoid the RHP pole calculation; and 3) the proposed Method 1 is applicable to the harmonic stability analysis of any ac systems, which are composed of both current-controlled and voltage-controlled

inverters with any structures including all the major connection types and meshed connections.

The novelty of the proposed Method 2 is: 1) the underlying principle of the impedance-based stability analysis using Cauchy's theorem is clearly identified; 2) the proposed Method 2 is a generalized extension of the impedance-sum-type criterion to be used for the harmonic stability analysis of any multibus ac systems based on Cauchy's theorem; and 3) the approach of using Bode plots in the positive frequency range with the consideration of the order difference between the numerator and denominator to determine the encirclement of the origin point (0, $j0$) is demonstrated.

Thanks to the low computation burden, the inverter controller parameters of multibus ac systems can be designed by repetitively applying the proposed harmonic stability methods, and presented as stability regions in the parameter space. The proposed analysis and design methods are verified by experiments of a two-area system and a meshed system with both voltage-controlled and current-controlled inverters.

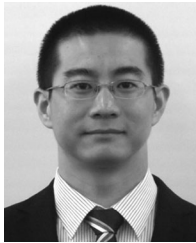
ACKNOWLEDGMENT

The authors would like to thank Dr. X. Zhang for his technical input.

REFERENCES

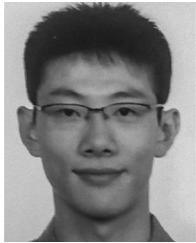
- [1] E. Muljadi *et al.*, "Equivalent the collector system of a large wind power plant," in *Proc. IEEE Power Eng. Soc. Gen. Meet.*, 2006, pp. 1–9.
- [2] J. M. Guerrero, M. Chandorkar, T. Lee, and P. C. Loh, "Advanced control architectures for intelligent microgrids—Part I: Decentralized and hierarchical control," *IEEE Trans. Ind. Electron.*, vol. 60, no. 4, pp. 1254–1262, Apr. 2013.
- [3] H. Wang, M. Wu, and J. Sun, "Analysis of low-frequency oscillation in electric railways based on small-signal modeling of vehicle-grid system in dq frame," *IEEE Trans. Power Electron.*, vol. 30, no. 9, pp. 5318–5330, Sep. 2015.
- [4] Z. Chen, Y. Luo, and M. Chen, "Control and performance of a cascaded shunt active power filter for aircraft electric power system," *IEEE Trans. Ind. Electron.*, vol. 59, no. 9, pp. 3614–3623, Sep. 2012.
- [5] F. Wang, Z. Zhang, T. Ericson, R. Raju, R. Burgos, and D. Boroyevich, "Advances in power conversion and drives for shipboard systems," *Proc. IEEE*, vol. 103, no. 12, pp. 2285–2311, Dec. 2015.
- [6] J. H. R. Enslin and P. J. M. Heskes, "Harmonic interaction between a large number of distributed power inverters and the distribution network," *IEEE Trans. Power Electron.*, vol. 19, no. 6, pp. 1586–1593, Nov. 2004.
- [7] P. Brogan, "The stability of multiple, high power, active front end voltage sourced converters when connected to wind farm collector system," in *Proc. EPE Wind Energy Chapter Semin.*, 2010, pp. 1–6.
- [8] A. A. A. Radwan and Y. A. I. Mohamed, "Modeling, analysis, and stabilization of converter-fed ac microgrids with high penetration of converter-interfaced loads," *IEEE Trans. Smart Grid*, vol. 3, no. 3, pp. 1213–1225, Sep. 2012.
- [9] X. Wang, F. Blaabjerg, and W. Wu, "Modeling and analysis of harmonic stability in an ac power-electronics-based power system," *IEEE Trans. Power Electron.*, vol. 29, no. 12, pp. 6421–6432, Dec. 2014.
- [10] X. Wang, F. Blaabjerg, M. Liserre, Z. Chen, J. He, and Y. Li, "An active damper for stabilizing power-electronics-based ac systems," *IEEE Trans. Power Electron.*, vol. 29, no. 7, pp. 3318–3329, Jul. 2014.
- [11] N. Bottrell, M. Prodanovic, and T. C. Green, "Dynamic stability of a microgrid with an active load," *IEEE Trans. Power Electron.*, vol. 28, no. 11, pp. 5107–5119, Nov. 2013.
- [12] C. Wan, M. Huang, C. K. Tse, and X. Ruan, "Effects of interaction of power converters coupled via power grid: A design-oriented study," *IEEE Trans. Power Electron.*, vol. 30, no. 7, pp. 3589–3600, Jul. 2015.

- [13] B. Wen, D. Dong, D. Boroyevich, R. Burgos, P. Mattavelli, and Z. Shen, "Impedance-based analysis of grid-synchronization stability for three-phase paralleled converters," *IEEE Trans. Power Electron.*, vol. 31, no. 1, pp. 26–38, Jan. 2016.
- [14] M. Salmani, N. Rahbari-Asr, C. S. Edrington, and C. Mo-Yuen, "Online and offline stability analysis methods for the power electronic-based components in design and operational stages," *IEEE Trans. Power Electron.*, vol. 31, no. 4, pp. 3151–3164, Apr. 2016.
- [15] P. Kundur, *Power System Stability and Control*. New York, NY, USA: McGraw-Hill, 1994.
- [16] N. Pogaku, M. Prodanovic, and T. C. Green, "Modeling, analysis and testing of an inverter-based microgrid," *IEEE Trans. Power Electron.*, vol. 22, no. 2, pp. 613–625, Mar. 2007.
- [17] J. He, Y. W. Li, D. Bosnjak, and B. Harris, "Investigation and active damping of multiple resonances in a parallel-inverter-based microgrid," *IEEE Trans. Power Electron.*, vol. 28, no. 1, pp. 234–246, Jan. 2013.
- [18] L. Hameforsi, X. Wang, A. G. Yepes, and F. Blaabjerg, "Passivity-based stability assessment of grid-connected VSCs—An overview," *IEEE J. Emerg. Sel. Topics Power Electron.*, vol. 4, no. 1, pp. 116–125, Mar. 2016.
- [19] Z. Liu, J. Liu, W. Bao, and Y. Zhao, "Infinity-norm of impedance-based stability criterion for three-phase ac distributed power systems with constant power loads," *IEEE Trans. Power Electron.*, vol. 30, no. 6, pp. 3030–3043, Jun. 2015.
- [20] J. Sun, "Small-signal methods for ac distributed power systems—A review," *IEEE Trans. Power Electron.*, vol. 24, no. 11, pp. 2545–2554, Nov. 2009.
- [21] B. Wen, D. Boroyevich, R. Burgos, P. Mattavelli, and Z. Shen, "Analysis of d-q small-signal impedance of grid-tied inverters," *IEEE Trans. Power Electron.*, vol. 31, no. 1, pp. 675–687, Jan. 2016.
- [22] M. Cespedes and J. Sun, "Impedance modeling and analysis of grid-connected voltage-source converters," *IEEE Trans. Power Electron.*, vol. 29, no. 3, pp. 1254–1261, Mar. 2014.
- [23] M. Belkhatay, "Stability criterion for AC power systems with regulated loads," Ph.D. dissertation, Dept. Electr. Comput. Eng., Purdue Univ., West Lafayette, IN, USA, 1997.
- [24] A. G. J. MacFarlane and I. Postlethwaite, "The generalized Nyquist stability criterion and multivariable root loci," *Int. J. Control*, vol. 25, no. 1, pp. 81–127, Feb. 1977.
- [25] B. Wen, D. Boroyevich, R. Burgos, P. Mattavelli, and Z. Shen, "Small-signal stability analysis of three-phase ac systems in the presence of constant power loads based on measured d-q frame impedances," *IEEE Trans. Power Electron.*, vol. 30, no. 10, pp. 5952–5963, Oct. 2015.
- [26] A. A. A. Radwan and Y. A. I. Mohamed, "Analysis and active-impedance-based stabilization of voltage-source-rectifier loads in grid-connected and isolated microgrid applications," *IEEE Trans. Sustainable Energy*, vol. 4, no. 3, pp. 563–576, Jul. 2013.
- [27] M. K. Bakhshizadeh *et al.*, "Couplings in phase domain impedance modelling of grid-connected converters," *IEEE Trans. Power Electron.*, vol. 31, no. 10, pp. 6792–6796, Oct. 2016.
- [28] A. Rygg, M. Molinas, Z. Chen, and X. Cai, "A modified sequence domain impedance definition and its equivalence to the dq-domain impedance definition for the stability analysis of AC power electronic systems," *IEEE J. Emerg. Sel. Topics Power Electron.*, vol. 4, no. 4, pp. 1383–1396, Dec. 2016.
- [29] J. Sun, "Impedance-based stability criterion for grid-connected inverters," *IEEE Trans. Power Electron.*, vol. 26, no. 11, pp. 3075–3078, Nov. 2011.
- [30] B. Wen, D. Boroyevich, R. Burgos, P. Mattavelli, and Z. Shen, "Inverse Nyquist stability criterion for grid-tied inverters," *IEEE Trans. Power Electron.*, vol. 32, no. 2, pp. 1548–1556, Feb. 2017.
- [31] Q. Ye, R. Mo, Y. Shi, and H. Li, "A unified impedance-based stability criterion (UIBSC) for paralleled grid-tied inverters using global minor loop gain (GMLG)," in *Proc. IEEE Energy Convers. Congr. Expo.*, 2015, pp. 5816–5821.
- [32] S. Lissandron, L. D. Santa, P. Mattavelli, and B. Wen, "Experimental validation for impedance-based small-signal stability analysis of single-phase interconnected power systems with grid-feeding inverters," *IEEE J. Emerg. Sel. Topics Power Electron.*, vol. 4, no. 1, pp. 103–115, Mar. 2016.
- [33] C. Yoon, H. Bai, X. Wang, C. L. Bak, and F. Blaabjerg, "Regional modeling approach for analyzing harmonic stability in radial power electronics based power system," in *Proc. IEEE Int. Symp. Power Electron. Distrib. Gener. Syst.*, 2015, pp. 1–5.
- [34] F. Liu, J. Liu, H. Zhang, and D. Xue, "Stability issues of Z + Z type cascade system in hybrid energy storage system (HESS)," *IEEE Trans. Power Electron.*, vol. 29, no. 11, pp. 5846–5859, Nov. 2014.
- [35] X. Wang, F. Blaabjerg, and P. C. Loh, "An impedance-based stability analysis method for paralleled voltage source converters," in *Proc. IEEE Int. Power Electron. Conf.*, 2014, pp. 1529–1535.
- [36] D. Yang, X. Ruan, and H. Wu, "Impedance shaping of the grid-connected inverter with LCL filter to improve its adaptability to the weak grid condition," *IEEE Trans. Power Electron.*, vol. 29, no. 11, pp. 5795–5805, Nov. 2014.
- [37] X. Wang, Y. W. Li, F. Blaabjerg, and P. Ch. Loh, "Virtual-impedance-based control for voltage-source and current-source converters," *IEEE Trans. Power Electron.*, vol. 30, no. 12, pp. 7019–7037, Dec. 2015.
- [38] M. Cespedes and J. Sun, "Mitigation of inverter-grid harmonic resonance by narrow-band damping," *IEEE J. Emerg. Sel. Topics Power Electron.*, vol. 2, no. 4, pp. 1024–1031, Dec. 2014.
- [39] K. Alawasa, Y. Mohamed, and W. Xu, "Active mitigation of subsynchronous interactions between PWM voltage-source converters and power networks," *IEEE Trans. Power Electron.*, vol. 29, no. 1, pp. 121–134, Jan. 2014.
- [40] L. Hameforsi, M. Bongiorno, and S. Lundberg, "Input-admittance calculation and shaping for controlled voltage-source converters," *IEEE Trans. Ind. Electron.*, vol. 54, no. 6, pp. 3323–3334, Dec. 2007.
- [41] X. Wang, F. Blaabjerg, and P. C. Loh, "Proportional derivative based stabilizing control of paralleled grid converters with cables in renewable power plants," in *Proc. IEEE Energy Convers. Congr. Expo.*, 2014, pp. 4917–4924.
- [42] Y. Gu, W. Li, and X. He, "Passivity-based control of dc microgrid for self-disciplined stabilization," *IEEE Trans. Power Syst.*, vol. 30, no. 5, pp. 2623–2632, Sep. 2015.
- [43] H. Liu and J. Sun, "Voltage stability and control of offshore wind farms with ac collection and HVDC transmission," *IEEE J. Emerg. Sel. Topics Power Electron.*, vol. 2, no. 4, pp. 1181–1189, Dec. 2014.
- [44] W. Cao, X. Zhang, Y. Ma, and F. Wang, "Stability criterion and controller parameter design of radial-line renewable systems with multiple inverters," in *Proc. Annu. IEEE Appl. Power Electron. Conf. Expo.*, 2016, pp. 2229–2236.
- [45] S. P. Rosado, "Voltage stability and control in autonomous electric power systems with variable frequency," Ph.D. dissertation, Dept. Electr. Comput. Eng., Virginia Polytech. Inst. State Univ., Blacksburg, VA, USA, 2007.
- [46] W. Cao, Y. Ma, X. Zhang, and F. Wang, "Sequence impedance measurement of three-phase inverters using a parallel structure," in *Proc. Annu. IEEE Appl. Power Electron. Conf. Expo.*, 2015, pp. 3031–3038.
- [47] L. Yang *et al.*, "Three-phase power converter based real-time synchronous generator emulation," *IEEE Trans. Power Electron.*, vol. 32, no. 2, pp. 1651–1665, Feb. 2017.
- [48] Y. Wang, X. Chen, Y. Zhang, J. Chen, and C. Gong, "Impedance modeling of three-phase grid-connected inverters and analysis of interaction stability in grid-connected system," in *Proc. IEEE Int. Power Electron. Motion Control Conf.*, 2016, pp. 3606–3612.
- [49] J. Wang *et al.*, "Static and dynamic power system load emulation in a converter-based reconfigurable power grid emulator," *IEEE Trans. Power Electron.*, vol. 31, no. 4, pp. 3239–3251, Apr. 2016.
- [50] X. Zhang, F. Wang, W. Cao, and Y. Ma, "Influence of voltage feed-forward control on small-signal stability of grid-tied inverters," in *Proc. Annu. IEEE Appl. Power Electron. Conf. Expo.*, 2015, pp. 1216–1221.
- [51] X. Zhang, X. Ruan, and C. K. Tse, "Impedance-based local stability criterion for dc distributed power systems," *IEEE Trans. Circuits Syst. I, Reg. Papers*, vol. 62, no. 3, pp. 916–925, Mar. 2015.
- [52] S. Liu, X. Liu, and Y. Liu, "Analysis on feedback interconnections of cascaded dc-dc converter systems," in *Proc. IEEE Energy Convers. Congr. Expo.*, 2015, pp. 5160–5166.
- [53] K. Ogata, *Modern Control Engineering*, 5th ed. Upper Saddle River, NJ, USA: Prentice-Hall, 2009.
- [54] F. Liu, J. Liu, H. Zhang, D. Xue, and Q. Dou, "Terminal admittance based stability criterion for multi-module dc distributed system," in *Proc. Annu. IEEE Appl. Power Electron. Conf. Expo.*, 2014, pp. 580–586.
- [55] F. Liu, J. Liu, H. Zhang, and D. Xue, "Generalized stability criterion for multi-module distributed dc system," *J. Power Electron.*, vol. 14, no. 1, pp. 143–155, Jan. 2014.



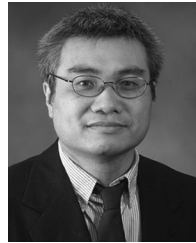
Wenchao Cao (S'13) received the B.S. degree in automation and the M.S. degree in control theory and control engineering from Huazhong University of Science and Technology, Wuhan, China, in 2008 and 2011, respectively. He is currently working toward the Ph.D. degree in electrical engineering at the Center for Ultra-Wide-Area Resilient Electric Energy Transmission Networks, Department of Electrical Engineering and Computer Science, College of Engineering, The University of Tennessee, Knoxville, TN, USA.

His research interests include stability of inverter-based power systems, modeling and control of grid-connected power converters, and motor drives.



Yiwei Ma (S'13) received the B.S. and M.S. degrees in electrical engineering from Tsinghua University, Beijing, China, in 2009 and 2011, respectively. He is currently working toward the Ph.D. at The University of Tennessee, Knoxville, TN, USA.

His research interests include modeling and control of power electronics interfacing converters for the renewable energy sources, multilevel converters, and microgrids.



Fred Wang (S'85–M'91–SM'99–F'10) received the B.S. degree in electrical engineering from Xi'an Jiaotong University, Xi'an, China, in 1982, and the M.S. and Ph.D. degrees in electrical engineering from the University of Southern California, Los Angeles, CA, USA, in 1985 and 1990, respectively.

He was a Research Scientist with the Electric Power Lab, University of Southern California, from 1990 to 1992. He joined the GE Power Systems Engineering Department, Schenectady, NY, USA, as an Application Engineer, in 1992. From 1994 to 2000, he was a Senior Product Development Engineer with GE Industrial Systems, Salem, VA, USA. During 2000 to 2001, he was the Manager of Electronic and Photonic Systems Technology Lab, GE Global Research Center, Schenectady and Shanghai, China. In 2001, he joined the Center for Power Electronics Systems (CPES), Virginia Tech, Blacksburg, VA, as a Research Associate Professor and became an Associate Professor in 2004. From 2003 to 2009, he was also the CPES Technical Director. Since 2009, he has been with The University of Tennessee and Oak Ridge National Lab, Knoxville, TN, USA, as a Professor and the Condra Chair of Excellence in Power Electronics. He is a founding member and Technical Director of the multiuniversity NSF/DOE Engineering Research Center for Ultra-Wide-Area Resilient Electric Energy Transmission Networks led by The University of Tennessee. His research interests include power electronics, power systems, controls, electric machines, and motor drives.